UNIVERSITÀ
DEGLI STUDI
DI PADOVA

UNIVERSITÁ DEGLI STUDI DI PADOVA

Dipartimento di Ingegneria Industriale DII

Corso di Laurea Magistrale in Ingegneria Energetica

Tesi di Laurea Magistrale in Ingegneria Energetica

THERMAL FLUID-DYNAMIC STUDY FOR THE THERMAL CONTROL OF THE NEW ALICE CENTRAL DETECTORS

STUDIO TERMO FLUIDO-DINAMICO PER IL CONTROLLO TERMICO DEI NUOVI RIVELATORI CENTRALI DEL PROGETTO ALICE

Supervisor: **Prof. Davide Del Col**

Co-supervisor: **Eng. Corrado Gargiulo**

Student: **Andrea Pelizzari**

Academic Year: 2016/2017

Abstract

The Inner Tracking System Detector of the ALICE Experiment at CERN laboratory will be replaced in 2020 with a new Detector. It will have to provide, among others, higher spatial resolution, higher tracking precision and faster data read-out. These goals will be attained thanks to new pixel sensors chips and new electronic components, which will have a high impact in terms of dissipated heat. Therefore, one of the critical aspects for the success of the Upgrade project is the design of the Detector cooling system.

This thesis work has been developed at CERN in Geneva in close contact with the group responsible for the Mechanics and Cooling of the Detector. The aim of the thermal fluid dynamic study devised is to deliver to the group a reliable and accurate description of the air flow inside the New Inner Tracking System Detector. After a first part of problem definition and design study, a Computational Fluid Dynamic (CFD) analysis has been developed with the ANSYS Fluent software.

The CFD model built in this work is a useful tool to predict the air temperature distribution and the air velocity inside the Detector in different operating conditions. This model allowed to explore various scenarios and optimize the in-detector cooling system design process. Furthermore, the optimization of the mass flow rate has provided important information and details about air cooling pipes number and diameter. In this sense, the ultimate purpose of the thesis is to support decisions about the design of the entire ALICE-Upgrade air circulation system.

Sommario

Il Tracciatore Interno dell'esperimento ALICE al CERN sarà sostituito nel 2020 con un nuovo Rivelatore, che dovrà garantire, tra le altre cose, maggior risoluzione spaziale, maggior precisione nel tracciamento e maggior velocità di processamento dei dati. Questi obiettivi saranno raggiunti grazie all'impiego di nuovi sensori a pixel e nuovi componenti elettronici, che avranno un forte impatto in termini di calore dissipato. Per questo motivo, uno dei punti critici per il successo del nuovo Tracciatore è la progettazione del sistema di raffreddamento.

Questo lavoro di tesi è stato sviluppato al CERN a Ginevra a stretto contatto con il gruppo responsabile della meccanica e del raffreddamento del Rilevatore. Lo scopo dell'analisi termo fluido - dinamica elaborata è quello di consegnare al gruppo una descrizione affidabile e precisa del flusso di aria all'interno del nuovo Tracciatore. Dopo una prima parte di definizione del problema e studio del progetto, è stata sviluppato un modello fluido-dinamico computerizzato tramite il software ANSYS Fluent.

Il modello costruito è un utile strumento per predirre la distribuzione della temperatura e della velocità dell'aria all'interno del Rilevatore considerando differenti condizioni di funzionamento. Esso ha reso possibile l'esplorazione di vari scenari e l'ottimizzazione del processo di progettazione del Tracciatore; inoltre, l'ottimizzazione del flusso di massa ha fornito importanti indicazioni circa il numero e il diametro dei tubi necessari per la ventilazione. In questo senso lo scopo ultimo della tesi è aiutare a prendere decisioni circa la progettazione dell'intero sistema di circolazione dell'aria all'interno di ALICE.

Contents

1

The Inner Tracking System Upgrade

The only true voyage of discovery, the only fountain of Eternal Youth, would be not to visit strange lands but to possess other eyes, to behold the universe through the eyes of another, of a hundred others, to behold the hundred universes that each of them beholds, that each of them is.

Marcel Proust [1]

Usually, in the public imagination, the word CERN evokes a world of strange particles, sometimes linked to God, secret experiments, new discoveries, most of the time intellectually unaffordable. The physicists' world, briefly. Therefore, usually, when I told someone that I was completing my master thesis in energy engineering there, two questions rose up; the first one dealt with my role as a student of engineering in an environment populated and dominated by physicists. The second one was related to my work and was like what I was trying to discover. Honestly, every time I didn't know how to answer these questions in a concisely and simple way, until I came up with a metaphor, suggested by Proust's famous quote written above. At CERN, some physicists of all over the world every day try to understand if they have found new pieces of their favorite puzzle, the Standard Model. Others struggle with enormous data sets to identify a hidden clue about the birth of the universe. These are *physicists'* voyages of discovery. Engineers don't search for new particles, they are not interested in seeking new universe landscapes. In the ocean of the knowledge, this is only the upper part of the iceberg. Engineers at CERN work underwater. Their aim is to exploit technology to see things from different points of view; their objective is to build detectors, new eyes to observe reality; their mission is to deliver to physicists new Inner Tracking Systems. This is *engineers* voyage of discovery.

1.1 Introduction

The thesis central issues are the thermal fluid-dynamic characterization of the air flow inside the new Inner Tracking System (ITS) and study of the optimal mass flow rate distribution. The entire dissertation is structured to move from the general context to the detail of the components.

In the first chapter an overview of the background is given, moving from CERN to ALICE experiment and finally to the new ITS. The aim of the chapter is to clarify what is the ITS, why a new one is needed and which are the main components.

The second chapter is focused on the air circulation. After an outline of the thermal requirements and the boundary conditions, a description of the air circulation system is provided, especially regarding the two main ITS components, the Inner Barrel (IB) and the Outer Barrel (OB). At the end of the chapter it will be clear why an air circulation system is needed and in which way the air will circulate inside the Detector.

The third chapter deals with the numerical model developed to study the air temperature and velocity distribution. The Computational Fluid Dynamic (CFD) approach is explained, in particular the pre-processing stage. It represents the level at which most of the uncertainties are introduced in the model, especially with simplified geometrical assumptions.

The fourth chapter is the core part of the thesis. Here the outcomes are shown and explained. Inside the Outer Barrel section, the results of simulation with different inlet nozzle diameter and different inlet velocity are provided. Then the result concerning the Inner Barrel and the Service Barrel are shown and explained. In the last section an assessment on the boundary condition parameters is given.

The conclusion highlights the most important outcomes in terms of temperature and velocity distribution, according to the identified optimal mass flow rate distribution among the components.

1.2 About CERN and LHC

The European Organization for Nuclear Research, known as CERN, is an European research organization active in the field of particle physics. Sometimes the term CERN is used also to refer to the complex system of laboratories located in the Geneva area, across the border between Switzerland and France. Established in 1954, CERN was one of Europe's first joint ventures and now has 22 member states. [2]

At CERN physicists and engineers are probing the fundamental structure of the universe through purpose-built particle accelerators and detectors. The accel-

erators boost beams of particles to high energy, at a speed very close to the speed of light; then particles are made to collide with each other and the detectors observe and record the results of these collisions. The collected data about collisions are processed and analyzed in loco and then spread around the world. [3]

Many activities at CERN currently involve the use of the Large Hadron Collider (LHC), that is the world largest and most powerful particle accelerator; it is the latest addition to CERN accelerators complex, started up on 10 September 2008. LHC consists of a 27-km ring of superconducting magnets, located 100 m underground. Inside the accelerator, two high-energy particles beams travel at close to the speed of light in opposite directions in separate beam pipes kept at ultrahigh vacuum. The beams are guided around the accelerators by a strong magnetic field maintained by special electromagnets; the magnets are built from coils of electric cable that operates in a superconducting state; this requires chilling the magnets down to 2 K, a temperature colder than the outer space. [4]

The beams inside the LHC are made to collide at four locations around the accelerator ring, corresponding to the position of four particle detectors that represents the main 4 experiments related to the LHC: ATLAS, CMS, ALICE and LHCb.

- ATLAS (A Toroidal Lhc ApparatuS) is dedicated to Higgs and Supersymmetry (SUSY) research.
- CMS (Compact Muon Solenoid) has the same purpose of ATLAS but different technical design
- ALICE (A Large Ion Collider Experiment) is designed specifically to study heavy-ion collisions in order to investigate the properties of the Quark Gluon Plasma (QGP).
- LHCb (LHCbeauty) is dedicated to the study of beauty quark production and asymmetry between matter and antimatter.

1.3 The ALICE Experiment

At the scale of atomic nuclei, protons and neutrons are bounded together by a force known as strong interaction; deep inside, in turn, protons and neutrons are composed by even smaller particles called quarks; quarks are bounded together by the same kind of force, the strong interaction, that is mediated by the exchange of force carrier particles called gluons. Nowadays the physics of strong interaction is well known, although there are two basic issues that remain unresolved rising two questions about the origin of confinement and the mechanism of the generation of mass. Regarding the confinement, no quark or gluon has ever been observed in isolation: they seem to be bound permanently together and confined inside particles, like protons and neutrons. Why? Regarding the generation of mass, it's well known that protons and neutrons are made of three quarks; nevertheless, adding together the masses of three quarks gets only about 1% of the proton or neutron mass. Why? [5]

The purpose of ALICE experiment (Figure 1.1) is to provide an experimental answer to the previous questions. In fact, the Quantum Chromo Dynamics (QCD), that is the current theory explaining strong interaction, predicts that at very high temperatures and very high densities quarks and gluons should no longer be confined inside particles but they should be free and separated in a new state of matter known Quark-Gluon Plasma (QGP). To achieve this kind of matter state the temperature has to exceed a critical value estimated to be around 2 000 billion degrees, about 100 000 times hotter than the core of the sun. And probably this was the temperature existing few millionths of a second after the Big Bang, when the entire universe was in quark-gluon plasma state. Thanks to the LHC, at CERN it's possible to accelerate in opposite directions two beams of heavy nuclei (Pb-Pb) at a speed close to that of light and then make them collide inside the ALICE detector. The nuclei collide and the extreme temperature releases the quarks and the gluons. Quarks and gluons collide with each other creating a thermally equilibrate state of matter: the quark-gluon plasma[6]

Figure 1.1: ALICE experiment logo [7]

1.3.1 ALICE detectors

As seen before, the key design consideration of ALICE is the ability to study Quark Gluon Plasma and quark confinement under these extreme conditions. So the main experimental challenge of the detector is to identify all the particles created inside the hot volume that live long enough to reach the sensitive detector layers situated around the interaction region. To be able to reach this goal, the ALICE experiment has been specifically designed to cope with multiplicities up to 8000 charged particles per rapidity unit at mid-rapidity, where rapidity is used as a measure for relativistic velocity. This is achieved by using 18 sub-detectors (Figure 1.2), each of them specialized in a set of measurements. The entire detector apparatus is divided in three main parts, covering different pseudorapidity η[1] intervals[8]:

- Central Barrel, covering the pseudorapidity region $\eta < 0.9$ [9].
- Muon Arm, covering range $-4 < \eta < -2.5$ [9].
- Forward Detectors.

The thesis is mainly focused on the central barrel detectors, in particular the Inner Tracking System (ITS). Other important detectors in the central barrel are the Time Projection Chamber (TPC), the Transition Radiation Detector (TRD) and the Time Of Flight (TOF). In addition, other three detectors with smaller acceptance are located at mid-rapidity: the High Momentum Particle Identification Detector (HMPID), the Photon Spectrometer (PHOS) and the electromagnetic calorimeters (EMCaL and DCal). All these detectors measure at many points the passage of each particle carrying an electric charge in order to give precise information about the particle trajectory and about the particle identity. To be able to derive particle momentum the ALICE barrel detectors are embedded in a magnetic field of 0.5 T provided by a huge and cold magnetic solenoid, powered by a 30 000 A current.

A specific description of the ITS will be performed in the next section, so, here, some basic information about the TPC, the TRD and the TOF will be given. The Time Projection Chamber (TPC) is a large volume filled with a gas

[1]Pseudorapidity $\eta = -ln(tan\frac{\theta}{2})$,where θ is the angle made by the particle trajectory with the beam pipe. Pseudorapidity is useful in LHC, where the composite nature of the colliding protons means that interations rarely have their centre of mass frame coincident with the detector rest frame, and where the complexity of the physics means that nu ifs far quicker and easier to estimate than rapidity (y). Furthermore, the high energy nature of the collisions mean that the two quantities may in fact be almost identical.

used as a detection medium: the charged particles that cross the TPC ionize the gas atoms in the surroundings and the atoms liberate electrons that drift towars the end plates of the detector. The characteristics of the ionization process can be used for particle identification. The Transition Radiation Detector (TRD), instead, is designed to identifiy electrons and positrons by the emission of transition radiation, X-rays emitted when the particles cross many layers of thin material with different dielectric constant. The Time Of Flight (TOF) gives the velocity of a charged particle by measuring the flight time over a given distance along the track trajectory.

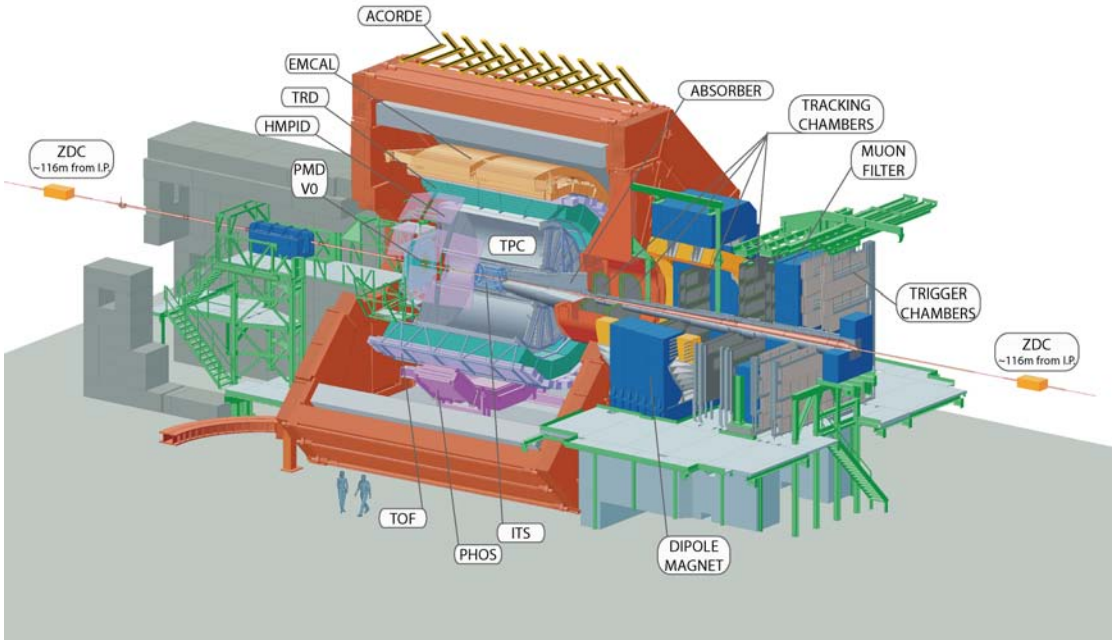

Figure 1.2: ALICE detectors layout [10]

1.3.2 The present Inner Tracking System

The Inner Tracking System currently in use (Figure 1.3) has a cylindrical symmetry around the beam axis, covering the total azimuthal axis. It is composed of six cylindrical layers of silicon detectors coaxial with the beam pipe to which it is anchored. The basic functions of the ITS are:

- determination of the primary vertex[2] and of the secondary vertices necessary for the reconstruction of quarks decays.
- Particle identification and tracking of low-momentum particles.
- Improvement of the momentum and angle measurements of the TPC.

As shown in Figure 1.3, the ITS is composed by two innermost layers (close to the beam pipe) equipped with Silicon Pixel Detector (SPD), two layers of Silicon Drift Detector (SDD) and lastly two layers of double-Sided Strip Detector (SSD). The SPD has a very important role in the determination of the coordinates of the primary vertex and in the measurement of the track impact parameters, that is crucial to split the tracks originated by weak decays (secondary vertices) from the tracks of the particles produced at the primary vertex [9]. The last four layers of the detector (SDD and SSD) provide energy loss measurements dE/dx thanks to their analog readout.

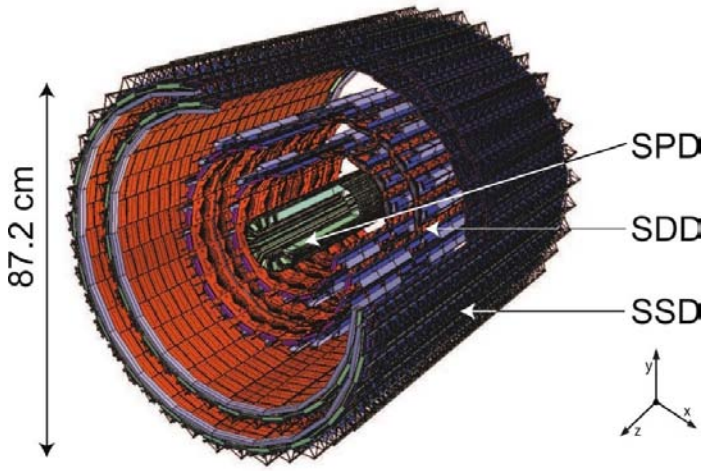

Figure 1.3: Inner Tracking System Layout [10]

[2]The primary vertex is the real high energy interaction point between particles; usually, from primary vertices secondary vertices are created due to weak decays.

1.4 The new Inner Tracking System

Some of the Quark-Gluon Plasma properties have been already studied at CERN SPS (CERN Super Proton Synchrotron) and at BNL RHIC (Brookheaven National Laboratory Relativistic Heavy Ion Collider) before the start-up of the LHC heavy-ion program and consequently prior to the start-up of ALICE. In only two years of Pb-Pb running the ALICE experiment has been able to confirm the basic picture of the measurements taken over the past decade, observing the creation of hot hadronic matter at un-precedent values of temperatures, densities and volumes with higher precision. Nevertheless the experiment is not yet fully optimized and further results could be achievable; ALICE capabilities can be enhnanced dramatically, unlocking the mysteries of QGP.

1.4.1 ALICE upgrade plans

The upgrade plans have been presented in the ALICE Upgrade Letter Of Intent (LOI), which was approved by the LHC Experiments Committee in September 2012. The LOI was followed by a Conceptual Design Report (CDR) that demonstrates that is possible to build a new silicon tracker with greatly improved features. In particular, the upgrades include:

- a new beam pipe[3] with smaller diameter;
- a new high resolution, low material Inner Tracking System (ITS);
- the upgrade of the Time Projection Chamber (TPC), consisting of the replacement of the wire chambers with Gas Electron Multiplier (GEM) detectors;
- the upgrade of the read-out electronics of Transition Radiation Detector (TRD), Time Of Flight detector (TOF) and Muon Spectrometer for high rate operations;
- the upgrade of the forward trigger detectors;
- the upgrade of the online systems and offline reconstruction and analysis framework;
- a new detector, the Muon Forward Tracker (MFT), consisting of five planes of silicon pixel detectors placed in front of the hadronic absorber;

[3]The beam pipe is the tube, kept in ultra vacuum, in which the beams travel.

Concerning the Inner Tracking System upgrade, a Technical Design Report (TDR) was presented after three years of Research and Development. The new ITS has to be able to read-out and record all the Pb-Pb interactions at 50 kHz and, in particular, to achieve the physics objectives, precise measurements at low transverse momentum are needed and, due to the increase of the integrated luminosity[4], high statistics is needed.

1.4.2 The ITS upgrade design objectives

In order to match the physics objectives the new ITS has to be developed with the following key-features:

- **First detection layer closer to the interaction point (IP)**; the reduction of the beam pipe radius in the center of the ALICE detector is crucial to achieve better measurement of the impact parameter resolution: it will be reduced from the actual 29 mm to 19 mm; thanks to this reduction, the first ITS detection layer radius will be lowered from 39 mm to 22 mm and the detection layers will be located between 22 mm and 400 mm. The outer radius is determined by the available volume inside the TPC bone and the necessity to compare tracks with those from the TPC.

- **Reduction of the material budget**; the problem related to the material budget is the effect of the multiple scattering which modifies the particle trajectory, deteriorating detector tracking efficiency. The use of Monolithic Active Pixel Sensors (MAPS) will allow the silicon material budget par layer to be dramatically reduced 7 times, from 350 μm (current ITS) to 50 μm. The MAPS technology allows also to optimize the pixel's power consumption, positively impacting the overall cooling and mechanics material budget of a factor of five.

- **Geometry and segmentation**; the overall detector main feature is the pixel sensor. A more precise position resolution can be achieved by lowering the dimension of the pixel size from 50 μm x 425 μm to 30 μm x 30 μm

- **Improvement of the tracking efficiency at low transverse momenta**; the upgraded ITS will have 7 layers instead of 6. This will improve the detector granularity, also thanks to the replacement of the SDDs and SSDs with pixel detectors.

[4]The number of events that an experiment observes is proportional to a quantity called luminosity. Higher luminosity means larger samples and better statistical accuracy

- **Fast read-out**; the benefit of measuring the ionisation in the silicon layers turns to be marginal compared to the overall results. So, the new configuration of the ITS will miss the particle identification feature and will be equipped with a binary read-out. In addition the upgraded ITS will have a huge improvement in the read-out capability, switching from a rate of 1 kHz to 100 kHz concerning the Pb-Pb collisions reading.

- **Fast insertion/removal for maintenance**; The design of the new ITS will be optimized in order to perform fast maintenance during the Year End Technical Stop (in event of detector modules damage).

1.4.3 The ITS upgrade Layout

The seven layers of the Inner Tracking System are grouped in two separate barrels, as shown in Figure 1.4: the Inner Barrel (close to the Beam Pipe) and the Outer Barrel. The Inner Barrel consists of three innermost layers (respectively called layer 0, 1 and 2) while the Outer Barrel consists of the four outermost layers (Layer 3 and 4, called Middle Layers and Layer 5 and 6, called Outer Layers)

Detector Stave Design

The ITS layers are segmented in the beam pipe direction in units named Staves. Each stave is mechanically independent and fixed to a support structure called End Wheel. The two End Wheels are split in two haves forming two Half-Layers. Every stave consist of the following elements, as shown in Figure 1.5:

- **Space Frame**: it is the light-weight carbon mechanical support structure of the stave itself;

- **Cold Plate**: it is the high-conductivity carbon plate structure in which the cooling pipes are embedded;

- **Hybrid Integrated Circuit (HIC)**: it is an assembly of poliymide Flexible Printed Circuit (FPC) on which the pixel chips are bonded (9 for Inner Barrel and 14 for Outer Barrel). For the Outer Barrel, this assembly is called Module.

- **Half Staves (HS)**: as stated above, staves are further azimuthally segmented in two halves, called Half Stave. Each half-stave consists of a number of modules (four for the Middle Layers and seven for the Outer Layers) glued on a common cooling unit;

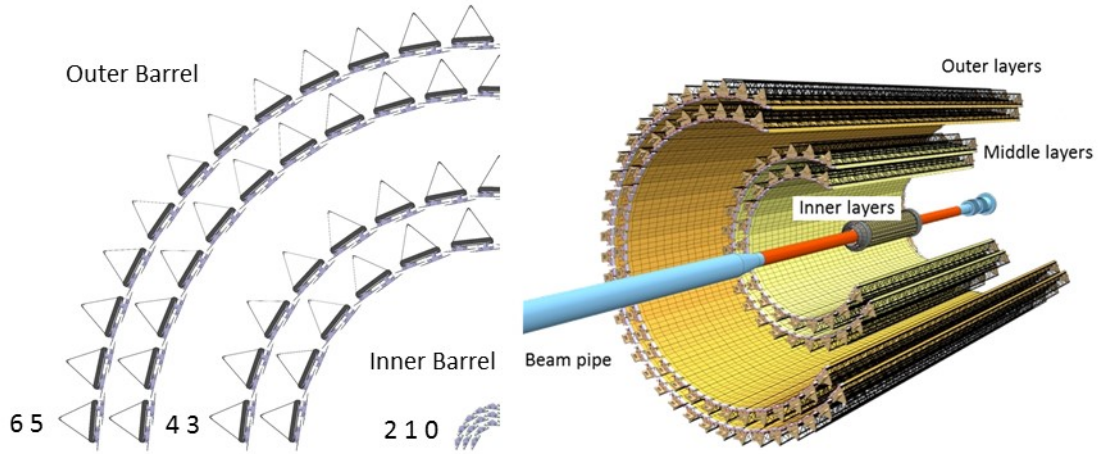

Figure 1.4: Layout of the new ITS detector [7]

Global support structure

As seen above, the Inner and the Outer Layers are held in position by two barrels, the Inner Barrel (IB) and the Outer Barrel (OB); the two barrels are supported by an integration structure named Cage, that covers all the length of the TPC bore. The global support structure is shown in Figure 1.6;

Detector Barrel Structure

The precise position of the staves in the barrels is provided by the End-Wheels (EW), light-composite end rings held in position by the Cylindrical Structural Shell (CYSS) for the Inner Barrel (Figure 1.7) and by the Conical Structural Shell (COSS) for the Outer Barrel (Figure 1.8).

Service Barrel Structure

All services, including cooling pipes, air ducts, power and signal cables will be integrated into the Service Barrels (SB) that are extensions of the Detector Barrels (DB). The Service Barrels have the same shape of the TPC cone: this is to distribute the services outside the acceptance of the forward detectors (Figure 1.9).

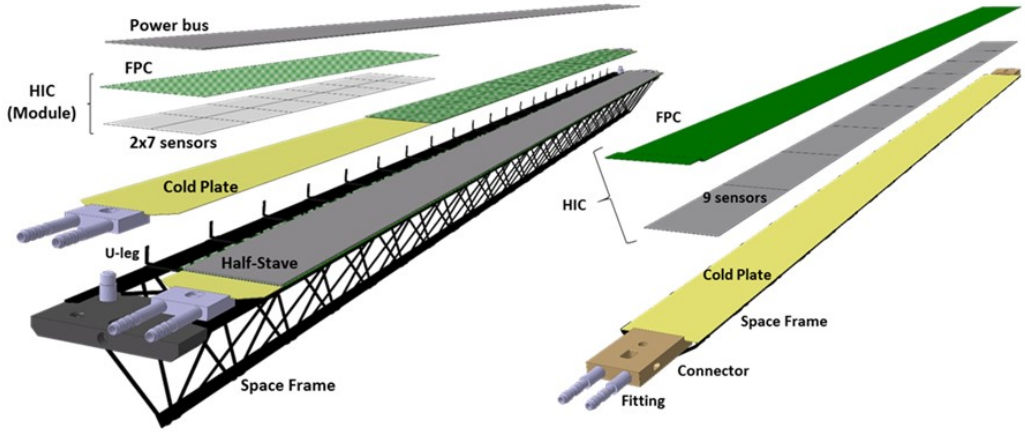

Figure 1.5: Inner and Outer Barrel stave design [11]

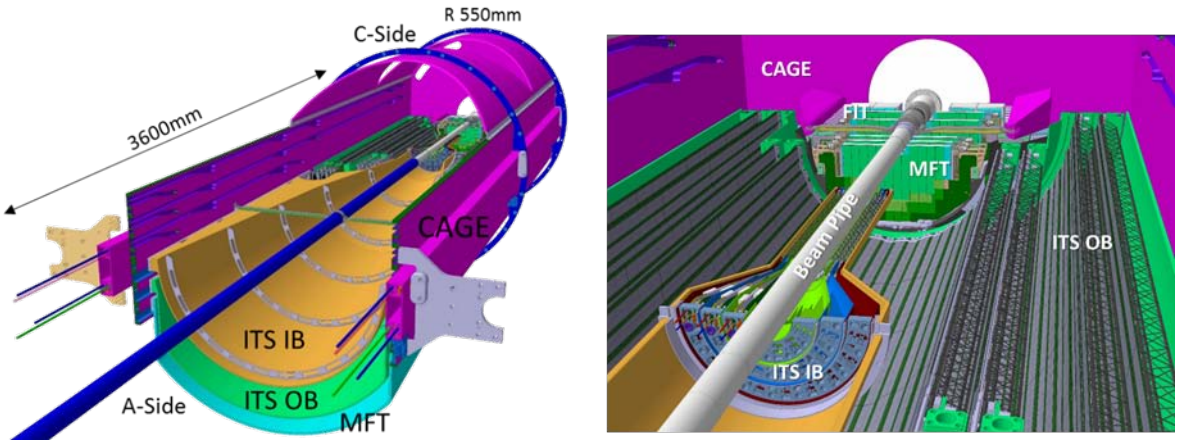

Figure 1.6: Global support structure design [11]

1.4.4 The Cooling System

The correct design of the cooling system plays a crucial role in the overall ITS upgrade success; indeed the sensors, the electronic and the mechanical components of the detector need to be cooled down or maintained at a proper value of the temperature. Particularly the cooling system should remove all the heat produced inside the detector by chips and services, remove all the heat produced by the off-detector electronics (like read-out systems), maintain the chips at the appropriate temperature in off-design conditions, avoid leaks and condensation inside and outside the detector and provide thermal insulation among the detectors (uniforming the temperatures); in addition the new cooling system must be compatible with the existing ALICE hardware and must comply with CERN and ALICE safety

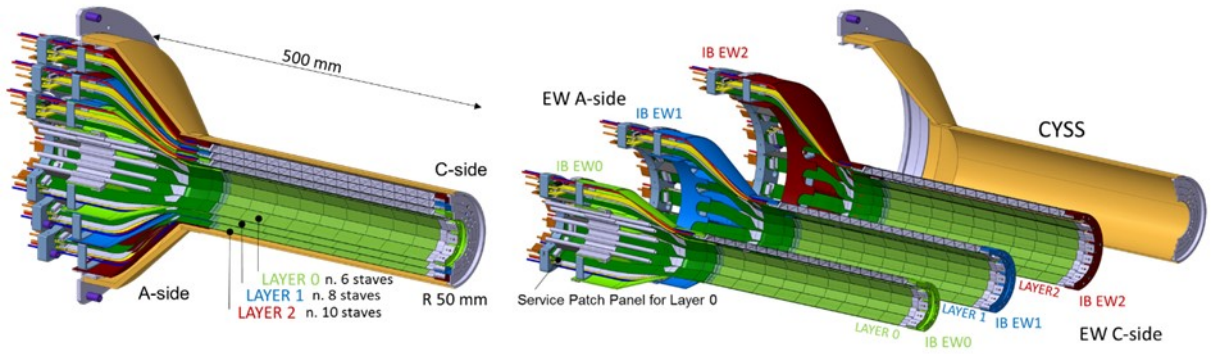

Figure 1.7: Inner Detector Barrel assembled and exploded [12]

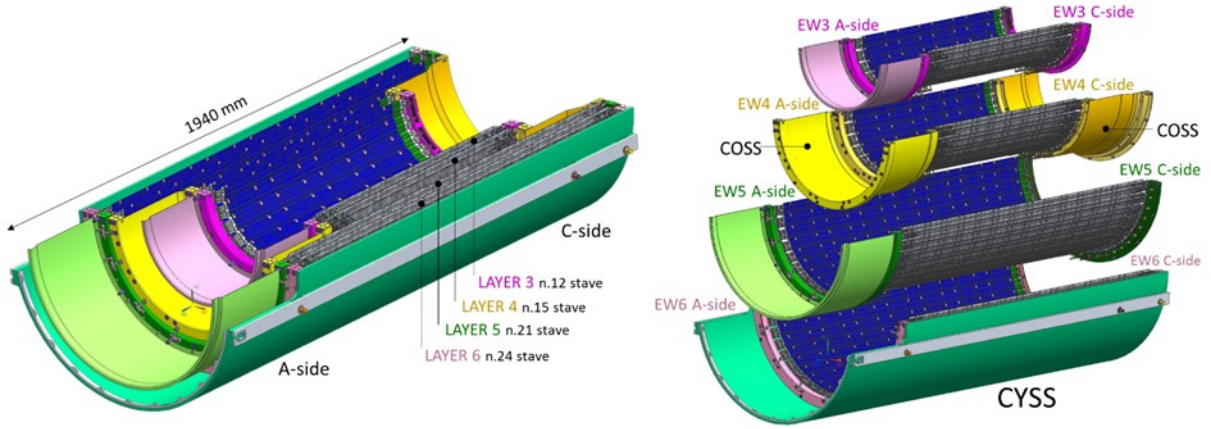

Figure 1.8: Outer Detector Barrel assembled and exploded [12]

regulations. In order to achieve the design objectives mentioned above, two cooling sub-systems are foreseen: a water cooling system, outlined below, and a air cooling system, precisely described in the next chapter.

Design Parameters

The cooling system design is driven by three key design parameters:

- Power Dissipation;
- Operational Temperature;
- Material Budget;

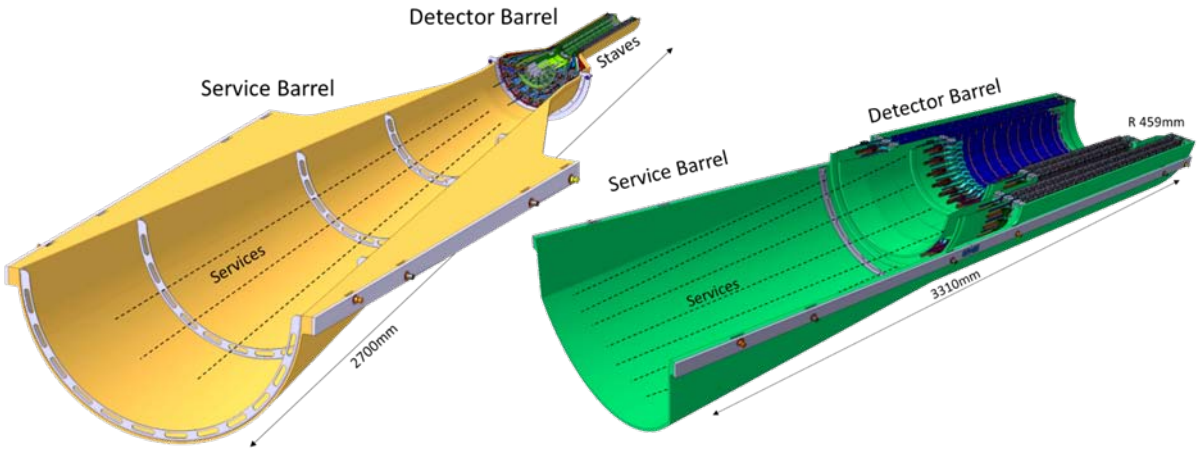

Figure 1.9: Service barrels [13]

Regarding the chip **power dissipation**, on the detector side there are three main heat sources: the chips, the buses and the power cables. The ALPIDE3[5] chip power dissipation has been experimentally checked and the value measured is 0.041 Wcm^{-2} for the Inner Barrel (IB) Staves chips and 0.028 Wcm^{-2} for the Outer Barrel (OB) Staves chips. With a safety factor of 50%, the considered specific power consumption turns out to be 0.061 and 0.042 Wcm^{-2} respectively for IB and OB. Considering the entire extension of the staves, the IB, MB and OB power consumption due to the chips are respectively calculated in ∼120 W, ∼1200 W and ∼3500 W. The power bus energy consumption consists of ∼26 W on the ML and ∼135 W on the OL. Finally, considering the cables dissipations, the ITS provides ∼34 W on the IB, ∼28 W on the MB and ∼46 W on the OL. Concerning the off-detector electronics, there's a power consumption of **1**0 kW (based on nominal 7.5 kW plus a safety factor). The overall ITS therefore dissipates roughly 15 kW.

As regards **operational temperature** and uniformity, the aim of the cooling system is to maintain the chip operational temperature below the threshold of 30°C. There is also a requirement concerning temperature distribution along the stave: the chip maximum temperature non-uniformity should be 5°C.

[5]ALPIDE: ALice PIxel DEtector is the pixel chip developed by a collaboration formed by CCNU (Wuhan, China), CERN, INFN (Italy) and Yonsei (South Korea). The key feature of the new chip is the low-power in-pixel discriminator circuit that drives an encoder read-out by a circuit. The digitalisation of the signal inside tha pixel eliminates the need for an analogue column driver, reduces the power consumption and allows for fast read-out

Concerning the **material budget**, the total IB layer material budget should be ∼0.3% and the total OB layer material budget should be ∼1%.

Boundary Conditions

The entire ITS is divided in two zones, as shown in figure: the A-side and the C-side. All the services to the detector come from A-side only, while the C-side is blind (closed by the MFT detector); so, all the pipes and the others services are routed along the service barrels. Another boundary condition is given by the dew point of the cavern, assumed to be 12°C: the minimum chip non-operational temperature (i.e the colder temperature reachable by the chip) should be above the dew point to avoid condensation on the surface of the chip. The entire cooling system should be, furthermore, very reliable: there is the need of a robust design with minimum mainteinance required. Finally, every material used for the cooling system should be compatible with the operation performed in the ALICE inner region.

Water Cooling System

The Water cooling system is responsible for detector and off-detector electronics cooling; concerning detector staves, each stave has an embedded cooling duct in the carbon cold-plate (Figure 1.10) and the heat is removed by leakless demineralised water with an inlet temperature range that varies between 18°C and 23°C. In regard of reliability, the water cooling system requires 3-4 times per year maintenance and the critical components are redundant.

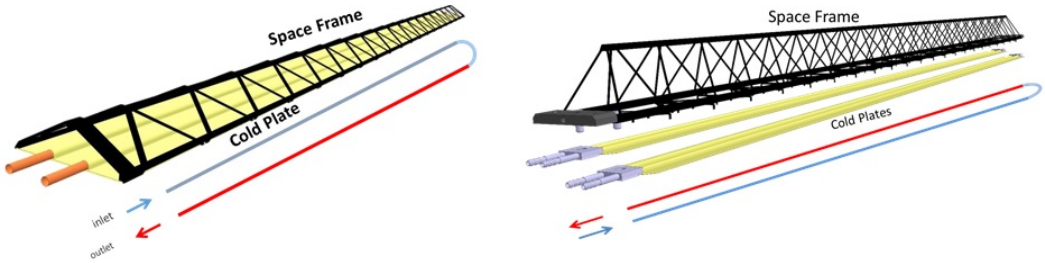

Figure 1.10: Inner Barrel and Outer Barrel stave cooling system layout [14]

2

The ITS Air Circulation

Our life is frittered away by details. An honest man has hardly need to count more than his 10 fingers, or in extreme cases he may add his 10 toes, and lump the rest. Simplicity, simplicity, simplicity.

Henry David Thoreau [15]

The starting point in the design process of the ITS air circulation layout was related to costraints and the boundary conditions. As in every engineering design project, at the beginning the only certainties were indeed the limits and the thresholds that can't be overcame. However, the requirements, sometimes, contradict each other. The heat in excess should be removed completely, but the air mass flow rate should be low; the air should reach the furthest point of the Detector, but the velocity should be under a certain value; the overall air circulation system should be effective and precise but totally reliable. So, at the beginning, different solutions and configurations have been tried, orienting the nozzles, moving them in the center of the Barrel, inserting additional pipes, controlling the mass flow rate of every End Wheel... However, developing the project, it became clear that every detail added has a negative influence on the entire ITS, in terms of mechanical stress, weight, physical space for the pipes; the more the level of detail rose, the less the system was reliable. It was at this moment that a new rule entered the minds of the team: *keep it simple*; from then on, every effort was addressed to obtain the maximum result with the minimum number of components. Simplicity, simplicity, simplicity.

2.1 Thermal Requirements and Boundary Conditions

The main purpose of the air circulation system is to maintain the overall temperature inside the detector as close as possible to constant and uniform conditions. Thus, to assure uniformity inside the barrel, the air flow must provide two services: it has to remove all the heat in excess not taken out by the water cooling system and it has to overcome the non-uniformity caused by the design geometry of the detector itself. The primary additional heat source is represented by the PowerBus while the most critical geometry non-uniformity is located in the transition zone in between Outer and Middle layers, where the staves length passes from 844 to 1500 mm.

2.1.1 PowerBus configuration

The description of the PowerBus can start from an etymological consideration: the term is composed by 'power' and 'bus', where 'bus' is the contraction of the latin ablative omnibus, that means 'for all'. Thus, PowerBus stands for 'power for all'. And finally this is its task: to bring power to all the electronical components lying on the staves. From that point on the abbreviation PB will be used referring to the PowerBus.

In order to figure out better the PB configuration, a deeper understanding of the stave upper design is needed. First of all, as mentioned above, there are two types of staves: Inner Barrel staves and Outer Barrel staves; the general design of these stave types is different and so also the service extension pattern varies.

Inner Barrel Service Extension

The Inner Barrel Staves are closer to the Beam Pipe and have strict requirements concerning material budget, weight and power dissipation, hence the IB service extension configuration is simpler that Outer Barrel one. As mentioned above, every stave extends for 844 mm and hosts 9 pixel chips, bonded on a Flexible Printed Circuit (FPC). Clearly every chip needs for electrical power, both for the analog circuit part and the digital circuit part, thus, there are two PowerBus: Analog PowerBus (APB) and Digital PowerBus (DPB). The service extension therefore is a multi-layer extension composed by the Flexible Printed Circuit, the Analog PB and the Digital PB, as can be seen in Figure 2.1.

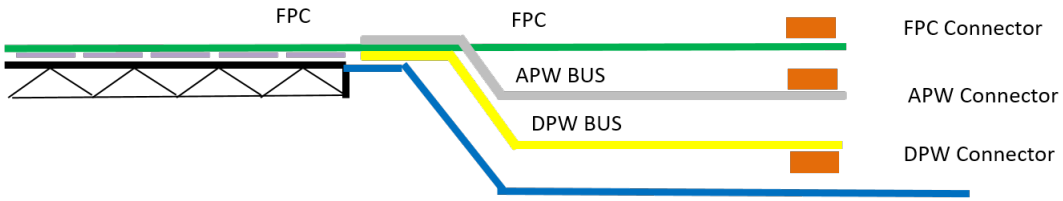

Figure 2.1: Inner Barrel multi-layer service extension [14]

Outer Barrel Service Extension

The geometry of the Outer Barrel staves is quite complex and also the OB service extension configuration is not simple as the IB one; as seen in the previous chapter, every Outer Barrel stave is split in two half staves, then also the service extension has to be split. In addition, alongside the Analogic and the Digital PB, there is another bus called Bias Bus. Thus, for every stave the multi-layer service extension is composed by double Bias Bus, double PB and double Flexible Print Circuit, distributed for every half stave as shown in Figure 2.2.

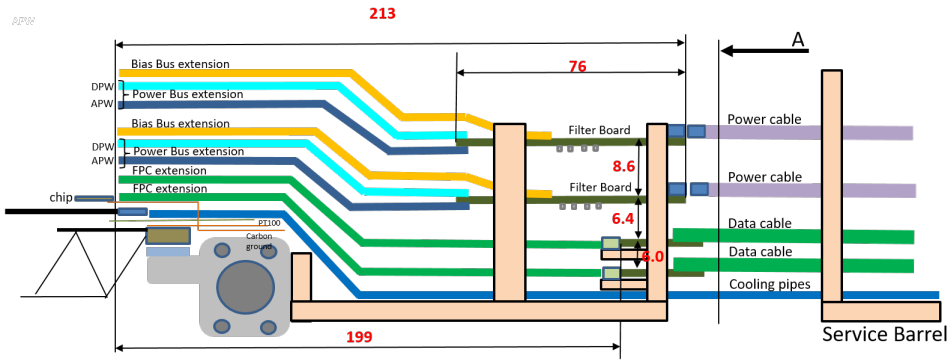

Figure 2.2: Outer Barrel multi-layer service extension [14]

The final stave configuration is shown in Figure 2.3 and Figure 2.4. The air-exposed part consists of a section of the upper PB surface, the entire Bias Bus and the Capacitors.

PowerBus and Bias Bus structure

The PB is composed of 5 alternate layers of conductive aluminum strips and dielectric kapton coverlays that work respectively as electric connections and grounding (Figure 2.4). The heat dissipation comes for Joule's effect from the electric power aluminum strips.

The Bias Bus, similarly, is composed of alternate layers of conductive aluminum strips and dielectric kapton coverlays and, as in the PB case, the heat dissipation comes for Joule's effect from the electric power aluminum strips.

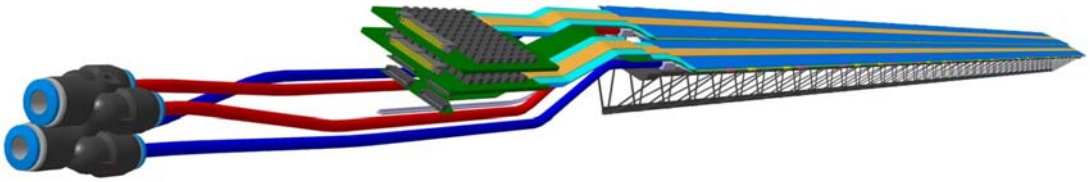

Figure 2.3: Outer Barrel multi-layer service extension [14]

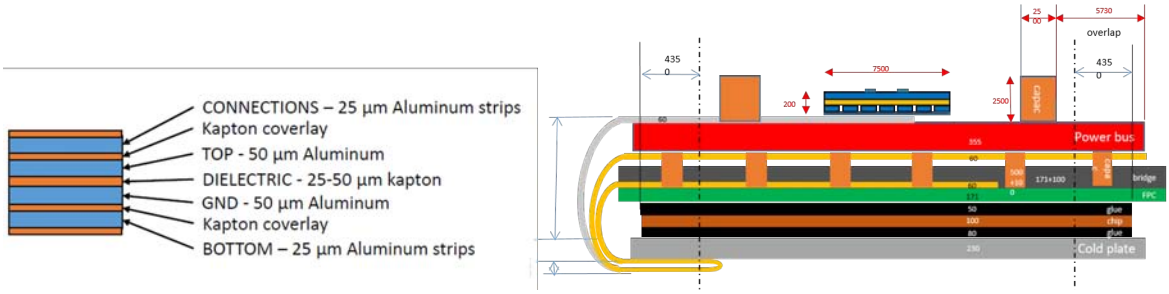

Figure 2.4: PowerBus section structure and stave transverse section [16][17]

2.1.2 Boundary Conditions

Thermal Boundary conditions

The overall power dissipated inside the detector is shown in Table 2.1. As can be seen, in the Outer Layers staves (L5 and L6) the dissipated power is higher than in the Middle Layer Staves (L3 e L4). Referring the powers of Table 3.1 to the stave area, the heat flux obtained is 19.54 W/m^2 for the Outer Layer staves and 9.87 W/m^2 for the Middle Layer staves. Regarding the Inner Barrel, the last experimental measurements have shown that the power dissipated by the IB PowerBus is close to zero and negligible. So, the only source of heat in the Inner Barrel will be the Beam Pipe after the High Luminosity Large Hadron Collider upgrade[1] and on the external surface there will be a heat flux of about 50 W/m^2. Concerning the Service Barrel, the dissipated power comes from the cables (Joule dissipation) and it is estimated as 34 W for the Inner Service Barrel (ISB) and 74 W for the Outer Service Barrel (OSB). Referring these powers to the surface extension covered by the cables, the heat flux obtained is:

- 9.4 W/m^2 for the ISB
- 19.6 W/m^2 for the OSB

Layer	N. of Staves	N. of Half-Staves	N. of HICs	Power Bus Dissipation (W)
L0	12	12	12	-
L1	16	16	16	-
L2	20	20	20	-
L3	24	48	192	12
L4	30	60	240	15
L5	42	84	588	72
L6	48	96	672	83
Total	**192**	**336**	**1740**	**182**

Table 2.1: PowerBus dissipated power in the detector side.

[1]The High Luminosity Large Hadron Collider (HL-LHC) is an upgrade to the Large Hadron Collider that should be operative from 2025. The upgrade aims at increasing the luminosity of the machine by a factor of 10, providing a better chance to see undisclosed processes and delivering better statistically measurement[18].

Air velocity Boundary conditions

The other boundary conditions inside the barrel are related to the stave stability: in order to give precise measurement the stave must stay still in position, therefore the air flow doesn't have to interfere with it producing dangerous vibrations. The most critical zones are located in the spaces between the half staves and the staves of the Layer 3 because all the mass of air flows through there and the space is very narrow (up to 0.834 mm), as shown in Figure 2.5;

To have a velocity threshold, a vibration test air flow has been performed and the result is that the stave has an acceptable displacement smaller than 3.6 μm for a velocity of 3.2 m/s. So, inside the barrel, considering a safety margin of around 30% a maximum velocity of 2 m/s, in the most critical point, can be considered acceptable.

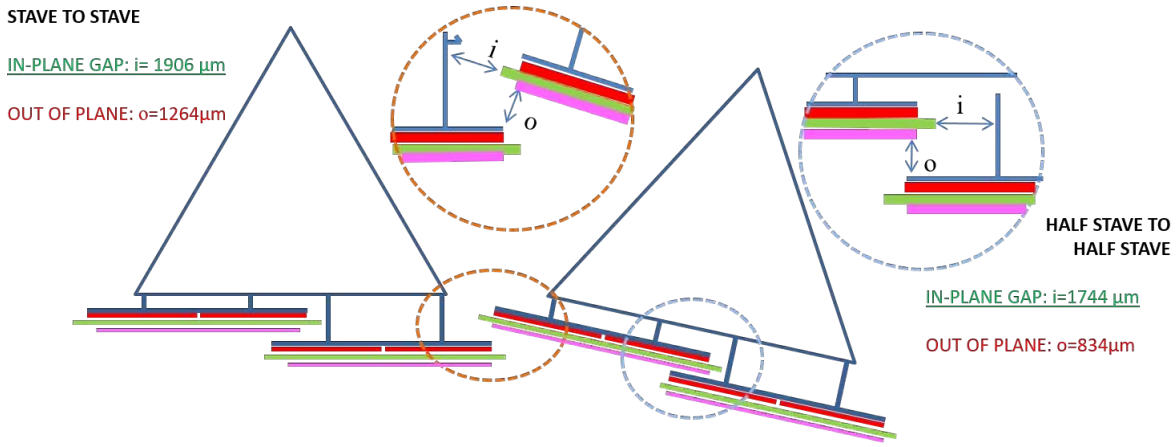

Figure 2.5: Stave and Half-Staves gaps [14]

2.2 Air Circulation System layout

The air circulation system in the ITS can be split in two zones: the detector-side air circulation, and the service side air circulation. The detector-side air circulation is the most important zone and it refers to the Inner and Outer Barrel air circulation. The service-side air circulation refers to the SB zone, where all the cables are placed. In both zones the air is blown by nozzles placed on a fundamental structure: the End Wheel (EW). As seen in the previous chapter, the principal task of every EW is to provide a precise position to the staves in the barrel, but they also work as air manifolds: the air ducts that come from the service barrel are connected to the EW and the air inside the EW structure is flushed in two opposite direction, one towards the detector barrel and one towards the service barrel (cf. 5.1.1, "Thermo-Fluid Dynamics Analysis: results - Using End Wheels as manifolds" for more information)

2.2.1 Outer Barrel air circulation layout

The air is introduced inside the barrel by nozzles placed on the End Wheels, both on A-Side and C-Side. On the A-Side End-Wheels there are 5 rows of nozzles. Counting from the outer row, there are (Figure 2.7, Figure 2.8 for the detail):

- 48 nozzles that flush the air under the Layer 6 ColdPlates
- 48 nozzles that flush the air over the 48 staves of the Layer 6
- 42 nozzles that flush the air over the 42 staves of the Layer 5
- 32 nozzles that flush the air under the Layer 4 ColdPlates
- 30 nozzles that flush the air over the 30 staves of Layer 4

On the C-side the pattern is the same but there is an additional row of 24 nozzles that flush the air over the 24 staves of Layer 3 (Figure 2.9).

The air enters the Outer Barrel in opposite directions from A-Side and from C-Side, then it's mixed with the Inner Barrel air and leaves the detector from the space between Inner and Outer Barrel.

The detector is accessible only from A-side, so the air is brought to C-side by air ducts that are routed between the cage structure and the Outer Barrel (Figure 2.6).

Figure 2.6: Air ducts from A-side to C-side [14]

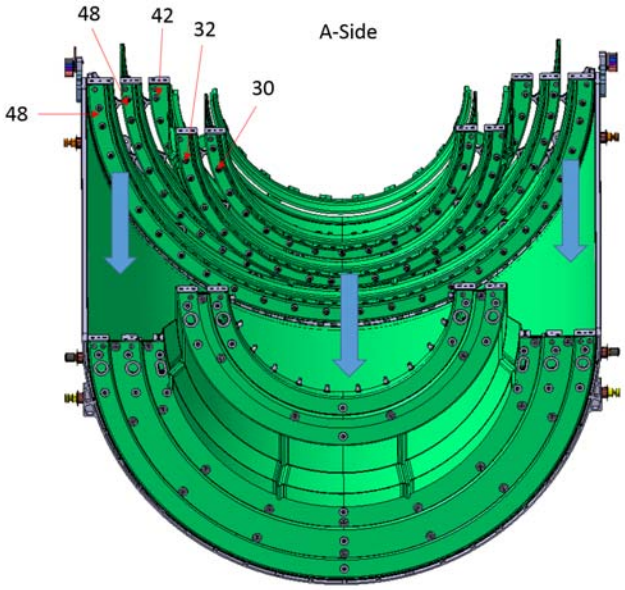

Figure 2.7: Outer Barrel Nozzles - A-side [14]

2.2.2 Inner Barrel air circulation layout

In the Inner Barrel the air is flushed from the Patch Panel placed at the end of the Conical Structural Shell, passes through the Inner Barrel Staves and finally reaches the center of the detector; here it is mixed with the Outer Barrel Air and exits into the service side. As can be seen in the Figure 2.10, there are:

- 10 nozzles (5 mm diameter) that flush the air inside the Conical Structure Shell

- 5 smaller nozzles (4 mm diameter) that by-pass the Shell cable-zone and flush the air directly in the space between the Beam Pipe and the first layer of staves.

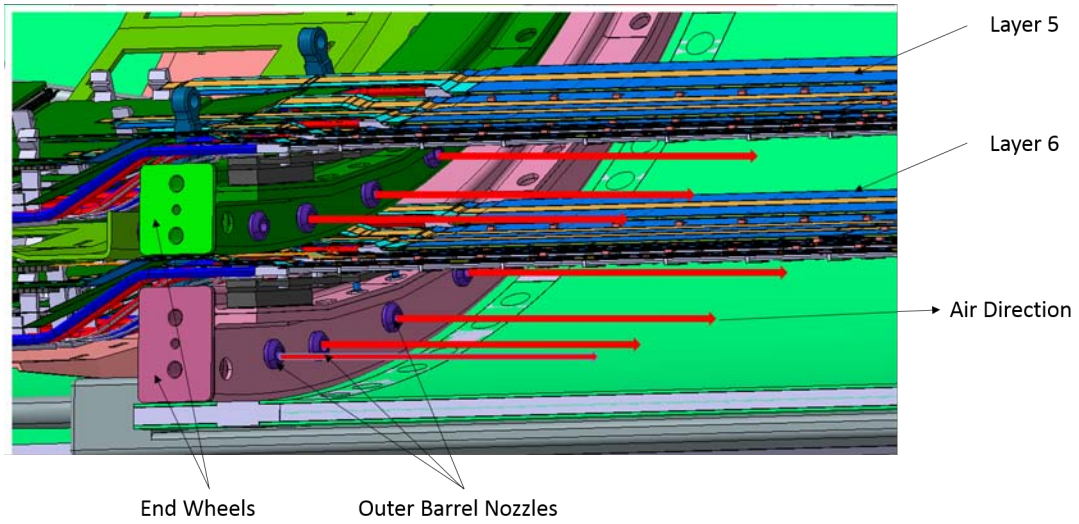

Figure 2.8: Outer Barrel Nozzles - A - side: detail and air trajectory [14]

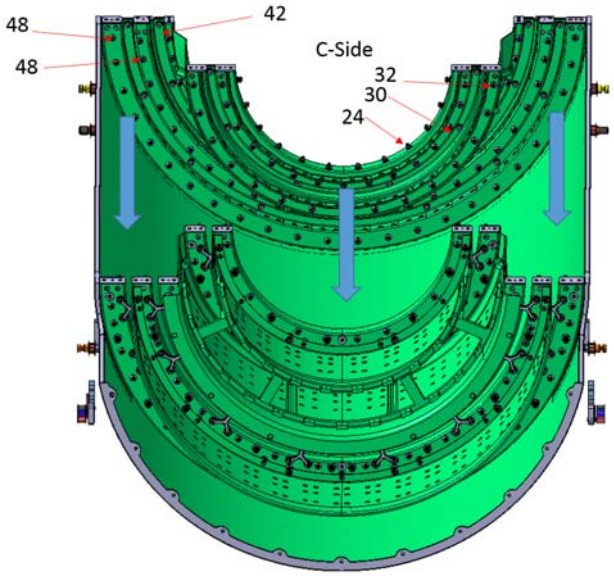

Figure 2.9: Outer Barrel Nozzles - C-side [14]

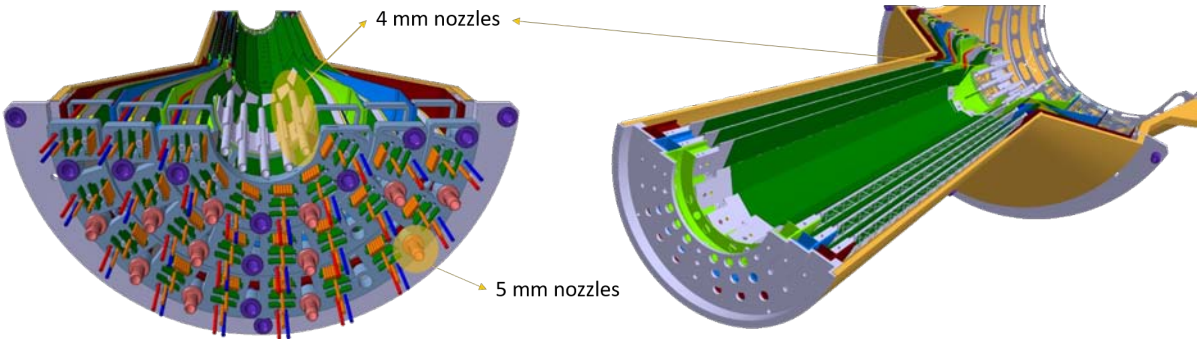

Figure 2.10: Inner Barrel air circulation Layout [12]

3 Numerical Model

I saw the angel in the marble and carved until I set him free.

Attributed to Michelangelo Buonarroti

The purpose of every numerical model is, on some level, foreseeing the future. Thus, engineers that try to simulate physical phenomena can be seen as a special kind of prophets that rely only on a well-known set of physical laws. But, luckily or unluckily, the whole reality is complex and complicated and can't be described only with a bunch of equations and constants. That's why Art exists. In order to have a reliable model, hence, a considerable reduction of complexity and complication is needed. The word 'Complex' comes from the Latin form 'Complexus', contraction of 'Cum-plexus', that means 'woven together'; 'complicated' instead derives for the Greek 'cum-plekéin' that means 'folded together'. So, reality is a complex system, characterised by its inter-dependencies and at the same time it's a complicated system, characterized by its levels folded together. In this context the engineer who wants to build a model has to take the whole reality and simplify it by limiting the inter-dependencies among the variables and reducing the layers of the object. He is like the artist, who try to shape a fine figure from a block of marble simply carving it and eliminating the marble in excess.

3.1 Model definition and project outline

The model described in this thesis aims to provide a reliable and accurate description of the air flow inside the Inner Tracking System. It must be seen as tool useful to predict the air temperature distribution inside the barrels in different operating conditions and explore various scenarios. The ultimate goal of the model is to

help taking decisions about the design of the entire ALICE-Upgrade air circulation system, providing answers to the following correlated questions:

- How many nozzles are needed in order to match the thermal requirements?
- Which is the optimal air flow, considering the existing air - circulation plant?
- Which is the optimal air inlet velocity?
- Are there hot spots on the layers? If yes, where?
- Are there critical points in terms of high velocity? If yes, where?

3.1.1 The Computational Fluid Dynamics approach

For the pourpose of answering the previous mentioned questions, a Computational Fluid Dynamics (CFD) approach has been followed. CFD solves partial differential equations (PDE) for conservation of mass, momentum and energy to predict fluid flow and heat transfer. The CFD software used for the model is ANSYS FLUENT (Release 17.2).

To solve the partial differential equations, the domain has to be discretized into a finite set of control volumes, as can be seen in Figure 3.1. The conservation equations are solved on this set of control volumes; thanks to this expedient PDE are discretized into a system of algebraic equations and then solved numerically to render the solution field.

The Computational Fluid Dynamics approach consists of four main operations:

- Problem and domain identification
- Pre - Processing
- Solving
- Post - Processing

3.2 Limiting the levels: Pre - Processing.

3.2.1 Assumptions on Geometry

Using directly the complete CAD models to extract the control volume is too expensive in term of computational power because the level of detail is too high. The first challenge, therefore, is to obtain a simplified geometry able to take in account of the most important features of the real one, without losing consistency. So the Staves, the Layers and the Barrels have been re-designed.

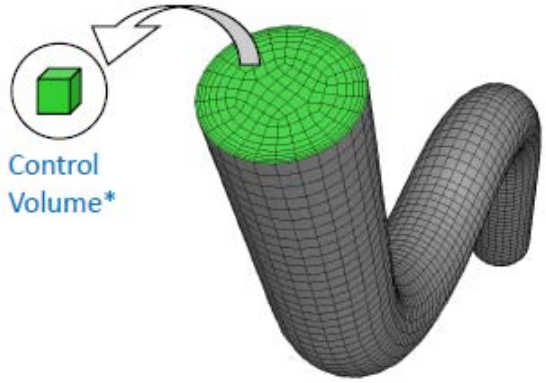

Figure 3.1: Discretization of the domain in a finite number of control volumes. [19]

Staves simplification

As seen above, staves are multilayer structures. For the purpose of the simulation, only the components of the stave in direct contact with the air are needed: PowerBus and ColdPlate, respectively the upper and the lower part of the assembly. The SpaceFrame is in direct contact with the air but its effects on air flow and thermal exchange are negligible. Regarding Outer Barrel staves, there is another simplification: in the real situation every stave is sliced in two half staves that are non complanar and at the in-plane distance of about 0.8 mm and out of plane distance of about 1.7 mm (Figure 3.2). In the model the stave is considered to be not sliced, as an entire part. The final stave considered in the model is a simple parallelepiped, and the two parallel rectangular plane faces represent the PowerBus and the ColdPlate.

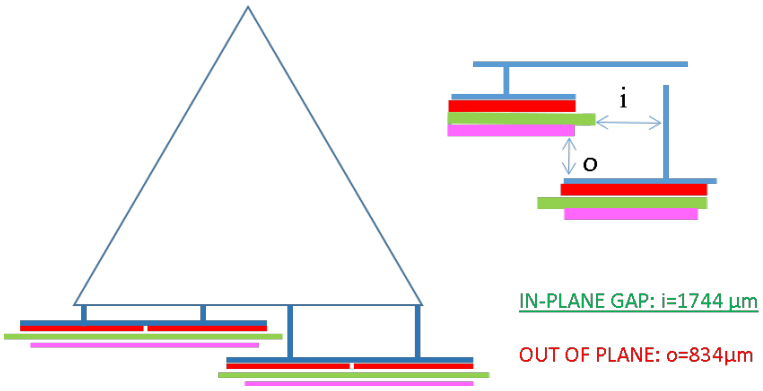

Figure 3.2: Outer Barrel stave structure: distances between half staves [14]

Layers simplification

Regarding the Layer, Inner Barrel and Outer Barrel models have to be distinguished. In the model of the Inner Barrel the relative position of the staves in the layer is the same of the reality. This because the overall extension of the IB detector side is lower and the importance of the relative position of staves can't be simplified, it is too important for the accuracy of the analysis. In the model of the Outer Barrel instead a simplification is needed. The real position of the staves in the layers is complicated since they are overlapped and very close each other (Figure 3.3). In the model the staves in the layers are not overlapped and distributed in-line. This means that the distance between every stave is not the real one, but it is increased by a factor of 1.5. The consequences of this assumption will be discussed later.

Barrels simplification

The analysis is entirely built on two levels of symmetry. The first level considers the half barrels, the second a symmetric section 3.5 of about 30° (cf. Chapter 4, section 4.3 "Outer Barrel: detector side results"). The reason of this is to lower the number of cells in the meshing procedure. Another simplification is performed at the level of the End Wheels: in the real design every EW is separated by a space, filled up with services and cables. The free space for the air flow between the cables is unknown and difficult to estimate, so in the model it is not considered (Figure 3.4): all the air flushed in the barrel by the nozzles exits from the space from Inner and Outer Barrel. Furthermore, using a symmetry of an angle of 30° between the planes (section of 1/12 of the entire) leads to a non integer number of nozzles for every row [1]. To overcome the issue and maintain a constant mass flow inlet and velocity using an integer number of inlets, nozzles of different surface are used. Also the geometry of the nozzles is modified: to achieve a better mesh, square nozzles are used instead of circular (keeping the same area).

3.2.2 Designing and Creating the mesh

As stated above, the equations are solved at cell locations. The process of dividing the fluid domain into discrete cells is called *Meshing*. To capture the flow features in high gradients zones and in fine geometrical details small cells are required and

[1] as can be seen in fig. 3.6 in the previous chapter, in the entire barrel, A-side, there are 5 rows of nozzles, from the outer EW to the inner one respectively 48, 48, 42, 32 and 30 nozzles. Taking a 30° symmetry, to obtain the number of nozzles in this section, every row has to be multiplied for the ratio 1/12. Thus, in the symmetry, counting the rows from the outer EW, row 1 and 2 must have $48/12 = 4$ nozzles, row 3 must have $42/12 = 3.5$ nozzles, row 4 must have $32/12 = 2.67$ nozzles, row 5 $30/12 = 2.5$ nozzles

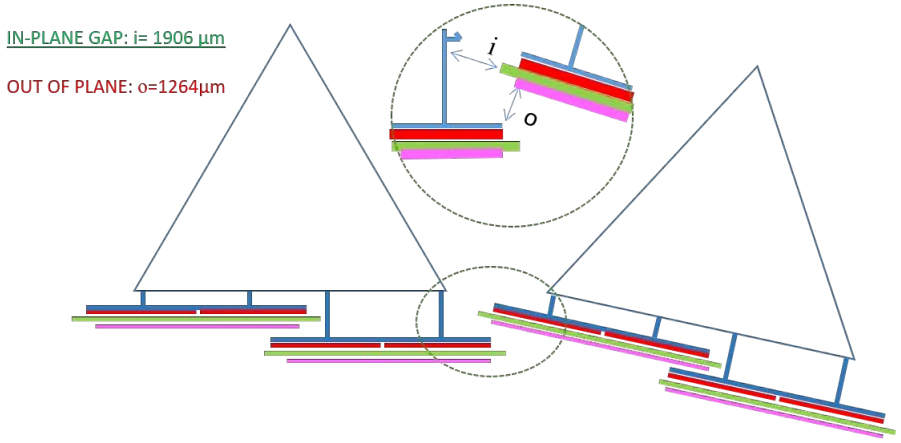

Figure 3.3: Outer Barrel stave structure: distances between staves [14]

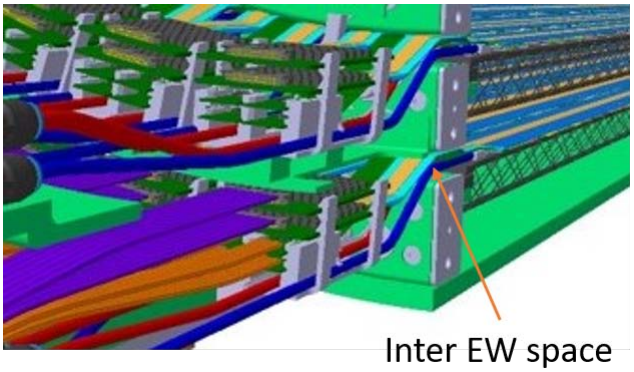

Figure 3.4: Space between End Wheels filled by cables and services- particular [13]

this leads sometimes to an elevated number of cells; that means high computational effort (because the number of cells is directly proportional to the number of points in which the features are calculated). To understand better the previous statement, the computer can be likened to the human brain: if the number of digits rises up, the ability to solve computations goes down due to human limited processing memory; that's why everyone can easily compute with a mental calculation the product *7 x 5* but not, for example, *758 x 862* with the same easiness. The computer brain (processor) has the same problems with its limited installed RAM memory. So, a good practice is to limit the count of cells, but it is challenging because some details need for a high number of cells to capture the particular feature. For example, to get an adequate information about the air velocity distribution between two half staves in Layer 3, at least four square cells in the space between are needed. The distance between the two half staves is about 0.8 mm,

this implies that every cell has to be *at least* 0.2 mm large. The half stave is 844 mm long, thus, finally, to have an accurate result, for every half staves 16880 cells are needed. That is too much in reference to the volume simulated and for this reason, as said above, the disposition of the staves in the layers has been simplified.

For this kind of reasons during the simulation different types of meshes has been used: pure structured hexahedral mesh inside the Outer Barrel (Figure 3.5) and unstructured tetrahedral mesh for the Outer Barrel and for the Service Barrel (Figure 3.6). The structured hexa mesh is composed of hexahedral regular cells and it allows to dramatically diminish the count of cells. Nevertheless, using this type of mesh, requires a strong geometry defeaturing and simplification. It has been used for the outer barrel because of the high volume at stake: using tet mesh would have led to a overmuch number of cells. By contrast in the Inner Barrel tet mesh has been preferred since the volume is less and the geometry is too complex to simplify.

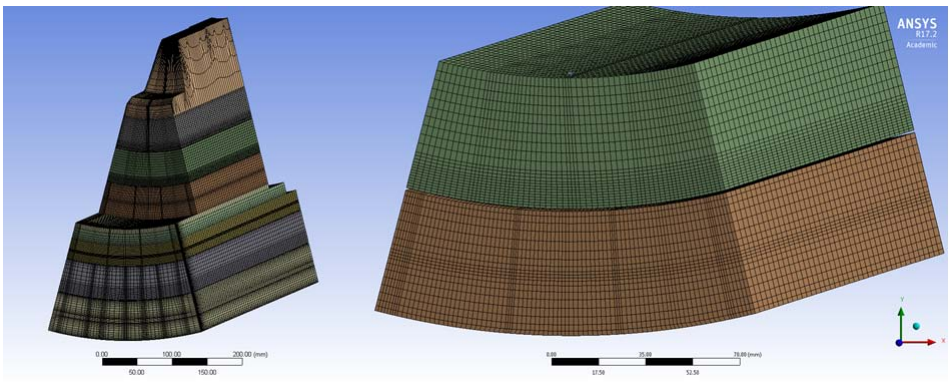

Figure 3.5: Outer Barrel Mesh: overview and particular

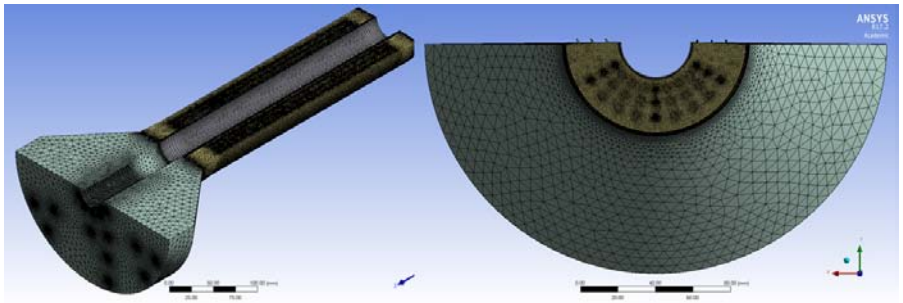

Figure 3.6: Inner Barrel Mesh: overview and particular

3.2.3 Outer Barrel Mesh validation

The temperature distribution inside the Outer Barrel is one of the most important parameters to consider in this simulation. For this reason a mesh validation process has been performed. The aim is to prove that the results given by the mesh (with the Fluent calculation) are accurate and achievable also with a different methodology. To prove it, first, the OB symmetrical mesh has been divided in 6 sub-mesh. The mesh between the Layer 6 and the Layer 5 is here used to explain the process (Figure 3.7).

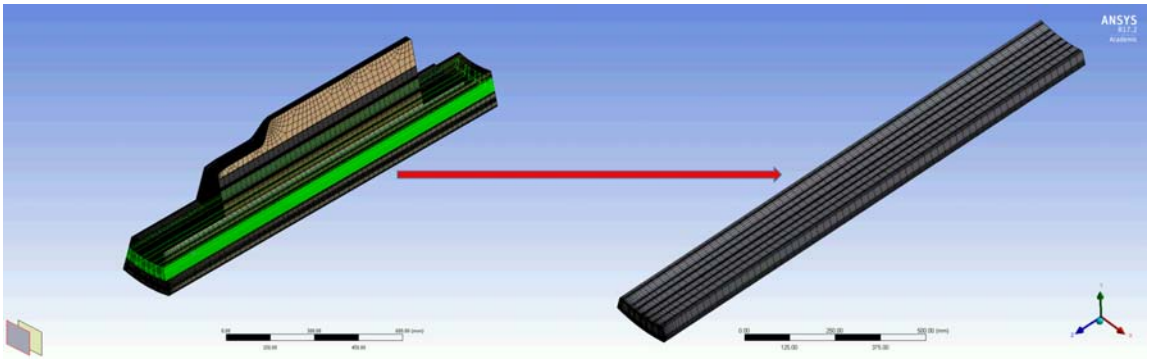

Figure 3.7: Mesh division: Layer 6 and 5 inter-mesh

To validate the simulation results given by the mesh, it has been used in Fluent to give results achievable also in another way. The shape of the mesh, indeed, is close to a rectangular duct. In this particular case there are some empirical correlation useful to calculate the local heat transfer coefficient and to compare it with the Fluent one. The air has been considered as an incompressible fluid with the properties at 23 $°C$ shown in Figure 3.8.

The simulation has been run in Ansys Fluent with Inlet Boundary conditions that assure fully developed turbulence (inlet velocity set at 20 m/s, inlet air T set at 300 K and constant heat flux from all the walls of the geometry set to 50 W/m^2).

The temperature and velocity values useful for the local comparison have been taken on a section plane placed in the fully-developed turbulence region, at a

c_p =	1006	[J/kgK]
nu =	0.00001838	[Pa s]
ro =	1.1922	[kg/m3]
k =	0.024	[W/mK]

Figure 3.8: Air properties at 23 $°C$

distance calculated according to the relation:

$$\frac{X}{L} = 20 \quad [20]$$

where X is the distance from the inlet and L is the hydraulic diameter:

$$L = \frac{4S}{P} \quad [20]$$

where S is the area of the section of the rectangular duct and P is the perimeter of the duct (Figure 3.9).

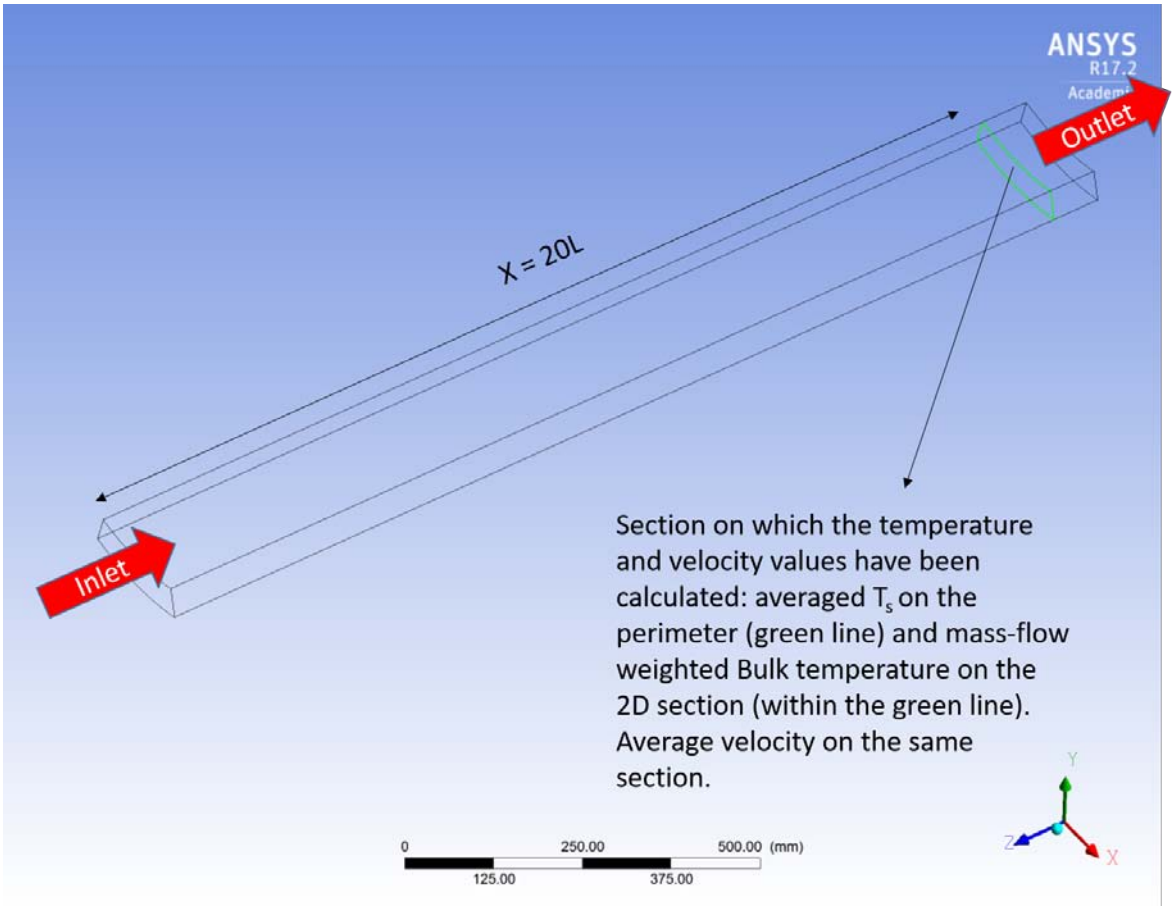

Figure 3.9: Outer Barrel considered mesh: highlighted in green the section at a distance equal to 20 times the hydraulic diameter

To calculate the first local heat transfer coefficient for the comparison the next relation has been use:

$$h = \frac{q}{T_s - T_b} \quad [20]$$

where T_s is the mean surface temperature, averaged on the green line highlighted in Figure 3.9 and T_b is the mean Bulk Temperature, obtained with a mass flow averaged function on the section on which the green line lies.

The result, with a heat flux of 50 W/m^2 are:

$$T_s = 301,02\ K$$

$$T_b = 300.16\ K$$

$$h = 58.2\ Wm^{-2}K^{-1}$$

.

To obtain a heat transfer coefficient for the comparison, the Pethukov and Gnielinski correlations have been used (both valid in the Reynolds range considered):

$$f = (0.790ln(Re) - 1.64)^{-2} \quad [21]$$

$$Nu = \frac{\frac{f}{8}(Re - 1000)Pr}{1 + 12.7(\frac{f}{8})^{0.5}(Pr^{0.67} - 1)} \quad [22]$$

The Reynolds and Prandtl numbers have been calculated with the relations:

$$Re = \frac{\rho u L}{\mu}$$

$$Pr = \frac{C_p \mu}{k}$$

Where u is the average velocity on the above chosen section.

The results are:

$$Re = 93672$$

$$Pr = 0.77$$

$$Nu = 180.3$$

From the Nusselt Number, the local heat transfer coefficient is obtained:

$$h = \frac{kNu}{L} = 57.5\ Wm^{-2}K^{-1}$$

.

As can be seen, the error between the local heat transfer coefficient obtained from Fluent (58.2 $Wm^{-2}K^{-1}$) and the local heat transfer coefficient obtained starting from Gnielinski correlation (57.5 $Wm^{-2}K^{-1}$) is very low (1.2%). The same calculation has been developed on all the sub-mesh and the error obtained is similar. So, from this, the conclusion is that the mesh used for the Outer Barrel simulation gives accurate results, compliant with the results obtained from an empirical correlation approach. The difference in the heat tranfer coefficients (around 1.2%) can be related to the geometry: the correlation used are valid for a rectangular duct while the mesh tested isn't a proper rectangular duct.

3.2.4 Limiting the inter-dependencies: physical model

Ansys Fluent basically solves conservation equations for mass and momentum. To deal with flows that involve other phenomena, like heat transfer or compressibility, additional sets of equations are solved (in the case of heat transfer the energy conservation equations).

The most important equations, common to every fluid flow simulations, are the Mass Conservation equation (Continuity equation) and the Momentum Conservation equations. They are applicable for a laminar flow in an inertial reference frame. To describe the turbulent flow in the near-nozzles area a Realizable k-ϵ model has been used (cf. Appendix A for more details about the mathematical model).

Heat transfers: Conduction

The thermal conduction has been modeled along the PowerBus length to take in account of the heat transferred along the aluminum electric conductor. Conduction heat transfer is governed by Fourier's law:

$$q_c = -k\Delta T$$

where q_c is the power transferred for conduction, k is the thermal conductivity and T is the temperature value. The thermal conductivity is a function of temperature and space automatically updated by the software. The Aluminum conductor is considered to be an isotropic material, so k doesn't change in spatial terms. In the pre-processing step, the stave (and the PowerBus) is not meshed (because for air convection and thermal radiation only the surface mesh is needed). Thus, to take in account of thermal conduction, the Ansys Fluent "Shell Conduction" option has been used. With this approach, a layer of virtual cells is created along the selected surface and heat conduction is calculated in the two perpendicular direction, as shown in Figure 3.10 .

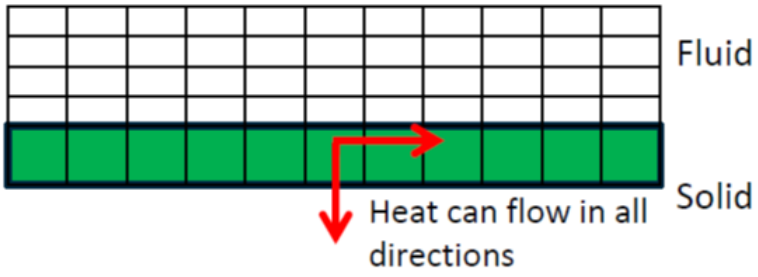

Figure 3.10: Shell conduction virtual cells creation [23]

Heat transfers: Convection

Convection heat transfer is strongly coupled to the fluid flow solution. The basic governing equation is the following:

$$q = h(T_b - T_i)$$

where the most important parameter is h, namely the average heat transfer coefficient. At the walls, the heat tranfer coefficient is computed by the turbulent thermal wall functions, included in the turbulent model mentioned above. (cf. Appendix A for more details about the equations used by Ansys Fluent).

Heat transfers: Thermal Radiation

In radiative heat transfer the energy is transported via electromagnetic waves. Usually, for semi-transparent bodies, radiation is a volumetric phenomenon. Nevertheless, in the model the bodies that exchange heat by thermal radiation (mainly PowerBus and ColdPlates) are opaque and therefore in this simulation is essentially a surface phenomenon since nearly all internal emissions are absorbed within the body. In the simulation, the media between the surfaces (air) has been considered as a non-partecipating media, namely scattering-related phenomena are neglected. For this kind of situation Ansys Fluent has in-built model called "Surface To Surface Model (S2S)". The method is based on the view factors calculation and presents N equations for N surfaces which can be cart into matrix form as:

$$[K]\{J\} = \{E\}$$

where K is the NxN matrix, J is the radiosity vector and E is the emissive power vector [24]. (cf. Appendix A for more detail about the Ansys Fluent S2S Model)

4

Thermo-Fluid Dynamic Analysis: results

Einstein: "You know, Henri, I once studied mathematics, but I gave it up for physics."
Poincare: "Oh, really, Albert, why is that?"
Einstein: "Because although I could tell the true statements from the false, I just couldn't tell which facts were the important ones."
Poincare: "That is very interesting, Albert, because, I originally studied physics, but I left the field for mathematics."
Einstein: "Really, why?"
Poincare: "Because I couldn't tell which of the important facts were true."

Reported by David Singmaster[25]

The new Inner Tracking System is going to be installed in the ALICE cavern in 2020; unfortunately, until that time, a complete experimental measurement of the air temperature inside the detector cannot be performed. For the moment, subsequently, there's no experimental validation of the model presented in the chapters before. The process used to get the outcomes presented in the next sections, therefore, has been a continuous and constant comparison between the numerical results offered by the CFD analysis and the expected logical results suggested by the experience and by the instinct. Every step further in the simulation opened new questions and new scenarios and every single unexpected value of temperature threatened the validity of the entire six-month long simulation. It has been a real dialogue, in the Greek sense of the term (dia - logòs, through - speech, reason) between Mathematics, (numerical CFD results), and Physics (expected logic results). Sometimes, indeed, I had to cope with plausible numerical results out of the hand-calculated predicted range; and in this cases, without the possibility of an empiric validation, I was floating in the sea of Uncertainty; I had passed so many hours wondering myself if the value was true or not and then, after some

mental- swims, I found a rock, a mathematical formula that let me validate the veracity of the result. However, later, I often discovered that the value was true but meaningless, negligible in respect of the simulation aims and I realized to have lost a lot of time. Other times instead I had got some results that I had believed to be crucial for the simulations itself, on which I based some further analysis. Nevertheless, moving forward with the study, I started to doubt about that values and little by little I became aware of the mistake I was making, considering as true, false values arising from numerical instabilities or mesh-related issues. And, one more time, I realized to have lost a lot of time. But, at the end, I think that it wasn't wasting time. This kind of experience leads me to understand better the human nature; sometimes, as human beings, we struggle with meaningless details, crashing against self-built walls and losing the sight of the whole. Other times, facing false meaningful results, unconsciously, we tend to project to the reality facts that we would like to be real, avoiding to confront the truth, like me with my "most wanted" temperature values. There's nothing to do, we are constantly subdued to cognitive biases. Therefore, like Einstein and Poincaré did, jump from Mathematics to Physics and from Physics to Mathematics could be a good solution to not lose direction and finally, to get a valuable simulation.

4.1 Mass Flow and Inlet Velocity hypothesis

The mass flow available for the ITS ventilation comes from an existing outside-placed air treatment unit already installed over the cavern of ALICE. The entire HVAC[1] system in this moment it is providing the air for the actual Inner Tracking System. Try to adapt the existent plant to the new detector is one of the challenge the team has to face. A total mass flow of about 200 m^3/h can be used for the air circulation system of the ITS (Inner Barrel and Outer Barrel, Detector and Cable side), the TPC-ITS envelope and the MFT detector. The only degree of freedom remaining concerns the air distribution among the components. Thus a study including different mass air flows has been has been performed. The other parameters related to the air flow rate optimization are the nozzles diameter, the inlet air velocity and the heat flux dissipated by the power buses. A primary dimensioning has been developed in order to get a general overview of the order of magnitude of the air distribution among the components; the results are shown in Figure 4.1. As can be seen, starting from this air flow distribution, there is a safety margin of more than 50 m^3/h (flushed into the cavern) that could be addressed to potential critical points inside the Inner Tracking System.

[1]HVAC is the acronym for Heating Ventilating Air Conditioning

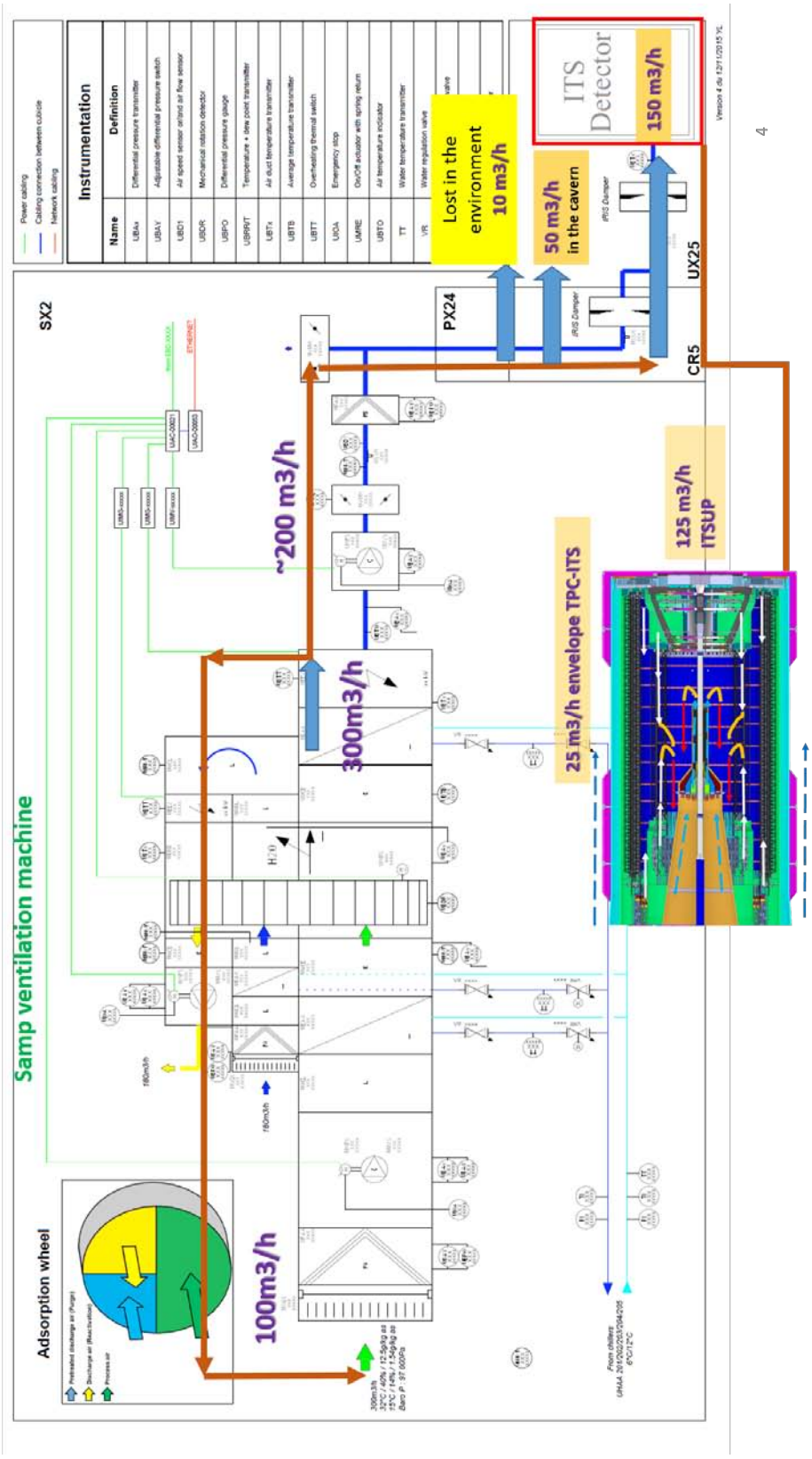

Figure 4.1: Air circulation available mass flow for the ITS-Upgrade [14]

4.1.1 Using End Wheels as manifolds

As described above, the air reaches the End-Wheels thanks to pipes directly fitted on the Inlet End Wheel Nozzles (IEN). The air enters the EW and leaves it in the opposite directions thanks to the Detector Barrel Nozzles (DBN) and the Service Barrel Nozzles (SBN) (Figure 4.2). The number of Detector Barrel nozzles and Service Barrel Nozzles is different (DBN are more than SBN) and for this reason the velocity inlet in the detector side is different that the one in the service side. The most important parameter to consider is the detector side inlet velocity and for this reason the service side velocity inlet depends on it and can't be varied independently. To study the velocity distribution on every detector nozzle, an End Wheel dedicated analysis has been developed. The results show that mass flow (and consequently, the velocity) is not perfectly constant for every nozzle but it depends on the closer Inlet End Wheel Nozzle position: DBN with IEN directly placed on the opposite side of the EW have higher velocities. Anyway, for the others analysis, the detector inlet velocity can be considered constant since the variation is negligible. For example, considering the End Wheel 6 with a standard mass flow inlet (the one considered for having an inlet velocity of 2.0 m/s in the detector side), the maximum velocity (reached in one of the 48 nozzles) is 2.08 m/s while the minimum velocity is 1.93 m/s with an average velocity for every nozzle of 1.99 m/s. The same situation occurs with the End Wheel 4, in which the maximum velocity predicted is 2.03 m/s and the minimum is 1.94 (avg 1.98 m/s). Regarding pressure inside the End Wheel, the simulation shows that there aren't critical situations, the air is a compressible gas and, furthermore, the number of outlets (DBN and SBN) is high. The maximum pressure increase inside the End Wheels is not above 10 Pa (respect to atmospheric pressure) and thus it is negligible.

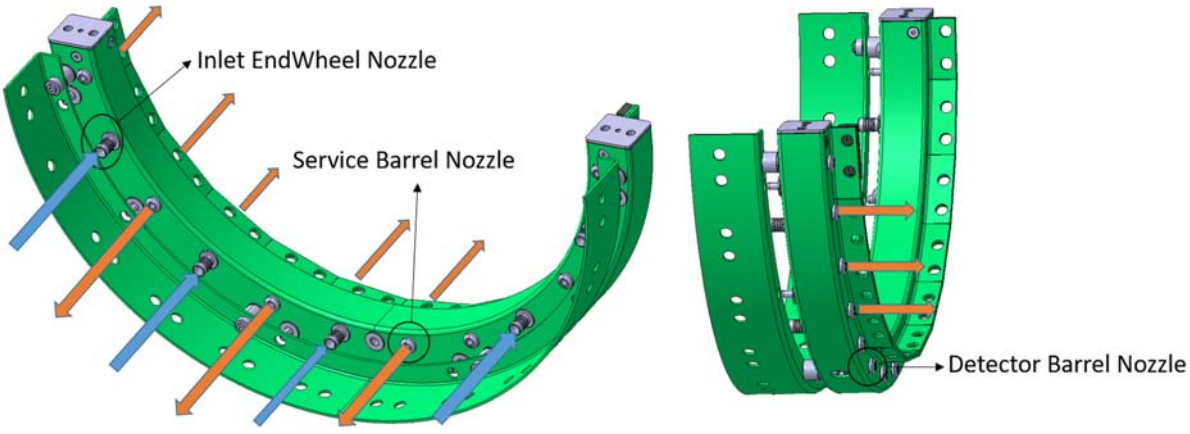

Figure 4.2: End-Wheel Layout [13]

4.2 Outer Barrel: Detector Side results

Concerning the Outer Barrel, the three heat transfer mechanisms have been simulated: thermal steady conduction along the PowerBus conductors, forced convection between the air and the PowerBus upper surface and thermal irradiation between the PB facing the ColdPlate of the next Layer. For the analysis, the half-barrel has been reduced to a symmetric 30° section (Figure 4.3). To obtain accurate results, a symmetrical hexa mesh has been used (cf section 3.2.2, Designing and creating the mesh). The inlets are placed in the lateral surfaces of the geometry (A side and C side, Figure 4.3) and the only unique outlet is located in the area between the Outer Barrel and the Inner Barrel.

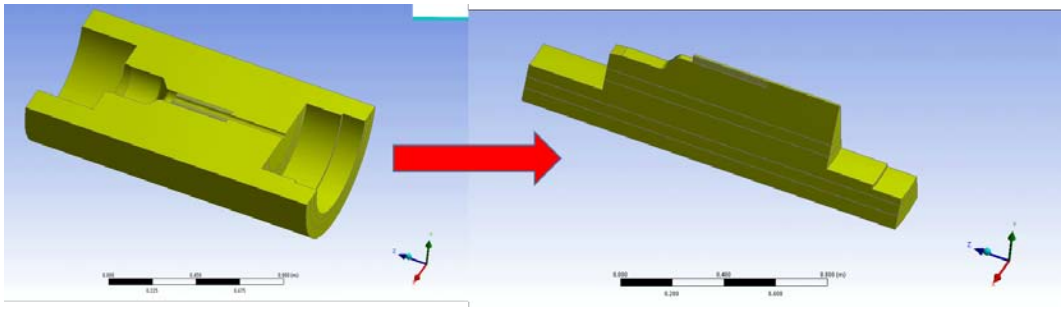

Figure 4.3: From the half-barrel to the 30° symmetric section

4.2.1 Boundary Conditions

The behavior of the temperature inside the Outer Barrel has been studied at different values of mass flow inlet, changing the inlet nozzles diameter (5 mm and 7 mm).

The other boundary conditions adopted are:

- constant heat flux from the PowerBus surfaces (respectively 20 W and 10 W/m^2 for Outer Layers and Middle Layers, for a total power of 181 W).
- constant ColdPlates temperature (20 °C).
- constant emissivity for both PowerBus and Coldplate surfaces (set at 0.7).

Concerning heat conduction, the conductors along the PowerBus are made of Aluminum, (thermal conductivity $\lambda = 290Wm^{-}1K^{-}1$) and have an average thickness of 0.115 mm. Regarding thermal irradiation, the PB is upper-covered

with a sheet of Kapton[2], the surface exposed of the ColdPlate is carbon fiber. Not having a direct measurement of the emissivity of the surfaces, average literature values has been used[3]($\epsilon = 0.7$).

4.2.2 Comparison between 5 mm and 7 mm nozzles

As stated above, the effect of mass flow rate on the temperature distribution has been studied for different nozzle diameters and different velocity inlets. A brief overview of the values at stake can be seen in Figure 4.4.

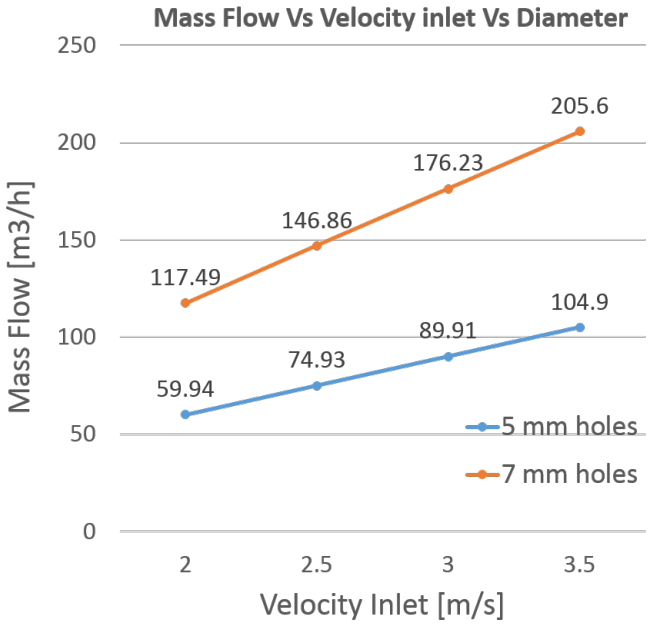

Figure 4.4: Relation between mass flow, velocity inlet and nozzle diameters

As can be seen, 8 different values of mass flow have been analyzed, ranging from 59.94 m^3/h to 205.6 m^3/h, related to 4 different velocity inlets: (2 m/s, 2.5 m/s, 3 m/s, 3.5 m/s) [4]. The mass flow curve related to the 7 mm nozzles is steeper because of the non-linear correlation between mass flow and nozzles diameter[5].

[2]Kapton is a poliymide film developed by DuPont in the late 1960s, commonly used in flexible printed circuits as electrical insulator [26]

[3]in the upcoming section, "Assessment on boundary conditions parameters", a detailed study about the emissivity value effect on temperature distribution has been developed

[4]Taking in account of the constraints explained in the previous chapter, only 4 design points can be suitable for the case: 5 mm nozzle at 2 and 2.5 m/s (respectively 59.94 and 74.93 m^3/h) and 7 mm nozzles at 2 and 2.5 m/s (respectively 117.49 and 146.86 m^3/h).

[5]$\dot{m} = v\rho\pi\frac{D^2}{4}$ where $\dot{m}$ stands for mass flow, v stands for velocity, and D stands for diameter

The maximum temperature reached in the barrel is a function of the mass flow inlet and, as expected, decreases with higher mass flow[6], (Figure 4.5).

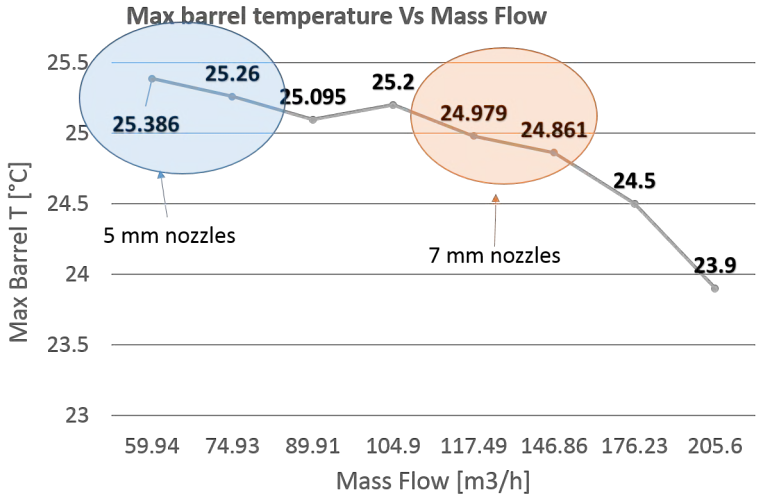

Figure 4.5: Relation between mass flow and maximum temperature inside the barrel

Figure 4.5 shows that, taking in account the boundary conditions explained above, a maximum temperature of $25.4°C$ is reached using the minimum velocity and mass flow values. Regarding the temperature gradient, the trend is the same and, for the available mass flows limited by the constraints, it varies from 5.5 C° to 5.00 C°. To a first approximation, switching from 5 mm nozzles to 7 mm nozzles and doubling the mass flow inlets (considering the same velocity) brings to a maximum temperature reduction of 0.41 °C (from 25.39°C to 24.98°C) and to a T gradient reduction of about 0.5°C

4.2.3 Air Velocity and Air Temperature Distribution inside the Barrel

The volumetric rendering of the air velocity distribution inside the barrel can be seen in Figure 4.6. From the volumetric plot, it is clear that in the central zone of the Outer Barrel the air is still, with a velocity close to zero. It can be explained by geometrical considerations: the region is quite far from the nozzles (that can be seen in the left and right zones) and so the air that reaches the zone has no

[6]simply from the first principle of thermodynamics, $\Delta T = \frac{P}{m \cdot c_p}$ where P stands for dissipated power and c_p is the air specific heat capacity, at the average simulation temperature $c_p = 1.005 \frac{kJ}{kgK}$

kinetic energy. Regarding the velocity distribution, Figure 4.7, transverse section taken exactly in the middle of the barrel, shows that the air velocity is higher in the upper part of the barrel, especially in the space between the staves in the same Layer and this can be explained referencing to the mass flow: all the air that enters the detector has to pass through space since the only air outlet of the detector is located in the upper part (between the Layer3 and the Conical Structural Shell of the Inner Barrel) and a high mass flow through a narrow area gives high velocity. So, as shown in the Figure 4.7, the critical point regarding maximum air velocity is in the space between the staves of Layer 3, as expected. The volumetric air temperature distribution inside the Outer Barrel can be seen in Figure 4.8;

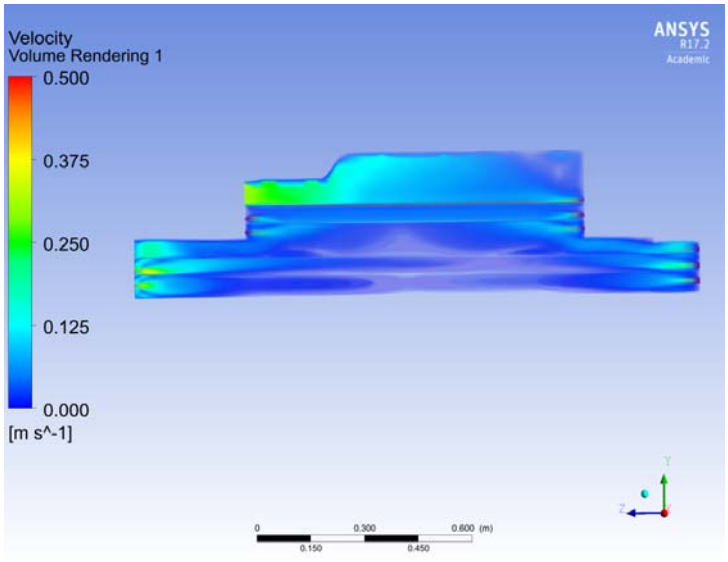

Figure 4.6: Volumetric air velocity distribution

the volumetric plot shows a hotter zone in the central part of the detector. Here the temperature is higher than in the rest of the barrel because the air reaches this region with a low velocity, as seen above. Thus, also the convective heat transfer coefficient is lower[7] and it leads to an increasing of the temperature. In the central zone of the detector, hence, the main part of the heat dissipated by the PowerBuses is removed by thermal radiation by the ColdPlate and then, at the end, by the water cooling system that keeps the ColdPlate at a constant temperature (at a value close to 20°C).

[7] $Nu = \frac{hL}{k} = CRe^m Pr^n, Re = \frac{\rho v d}{\mu}$

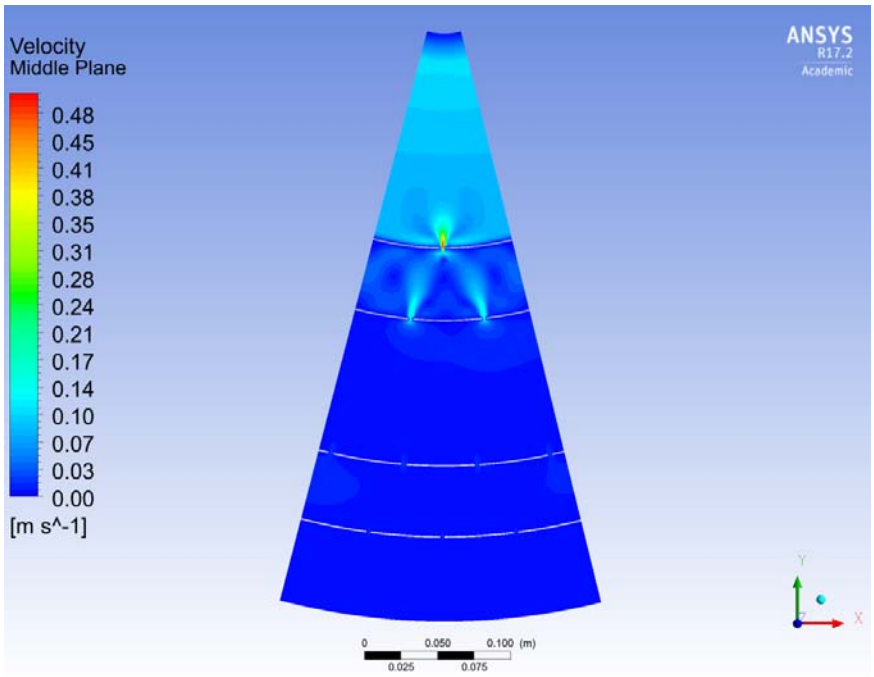

Figure 4.7: Transverse section air velocity distribution

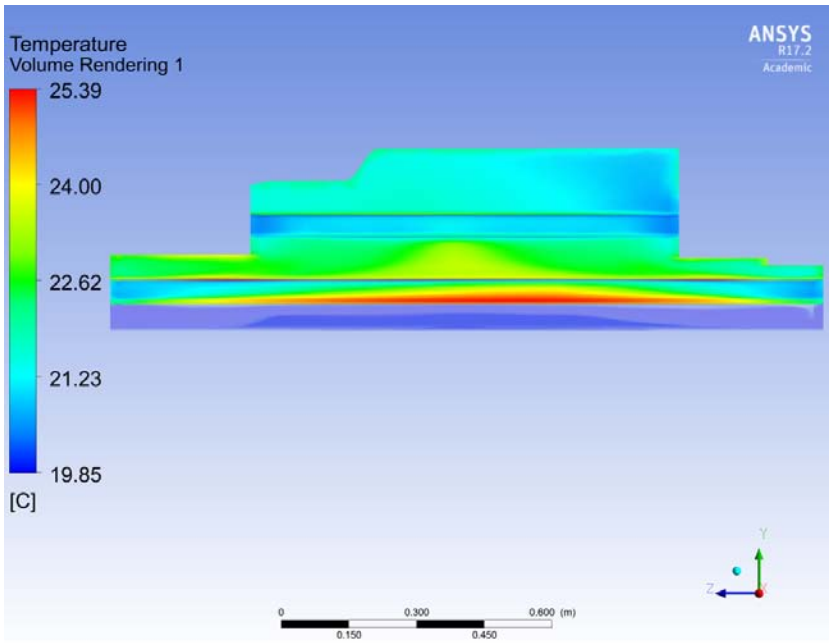

Figure 4.8: Volumetric air temperature distribution

4.2.4 Temperature profiles on the Staves

Two important parameters to verify with simulations are the maximum temperature reached and the distribution of the temperature along the surface of the PowerBus. As explained above, in the design conditions the max temperature and the temperature non-uniformity must stay in a defined range and can't exceed the limits. Concerning maximum temperature, it can't exceed the threshold of 26°C. Regarding the temperature non-uniformity, the reasonable temperature gradient along the stave should not exceed the 5°C. In Figure 4.9 the temperature distribution along Layer 3 and 4 can be evaluated: the maximum temperature reached by the PowerBus surface (respectively 22.83°C and 22.45°C) is widely below the threshold value, as well as the temperature gradient (respectively 1.87°C and 1.29°C). Observing Layer 3 temperature distribution, the lower temperature region is located in the C-side zone (bottom part of the figure). This can be explained by the particular geometry over the Layer 3: from the C-side there are the 24 nozzles that flush the air, from the A-side there is the outlet. So, in the A-side there aren't nozzles that directly provide fresh air to the layer and as consequently the temperature rises. Observing Layer 4, the higher temperature zone is located in the central part: as stated above, the central zone is poorly reached by the air and the temperature here tends to rise.

Concerning the Outer Layers, the results are shown in Figure 4.10: Also in this case (Layers 5 and 6) the temperature constraints have been respected: the maximum temperature values are respectively of 25.20°C and 25.09°C while the temperature gradient is of 3.41°C and 4.44°C. The figure clearly shows that the effect of the air is greater near the inlet zones. Considering the higher temperature level of the Outer Layer in respect of the Middle Layer, an explanation can be provided referring to the geometry of the layers: the staves of Layers 5 and 6 are longer that the staves of Layers 3 and 4 (1500 mm against 844 mm) and the specific heat flux is higher (20 W/m^2 against 10 W/m^2), so the power dissipated is greater (155 W against 27 W). Furthermore, the air flow in the upper part of the detector is larger because of the unique outlet situated on the A-side between the layer 3 staves and the Structural Shell of the Inner Barrel: all the air that enters the detector has to pass over the layer 3 and 4 to exit, while the only air over layer 5 and 6 is flushed by the respective stave nozzles, as explained above.

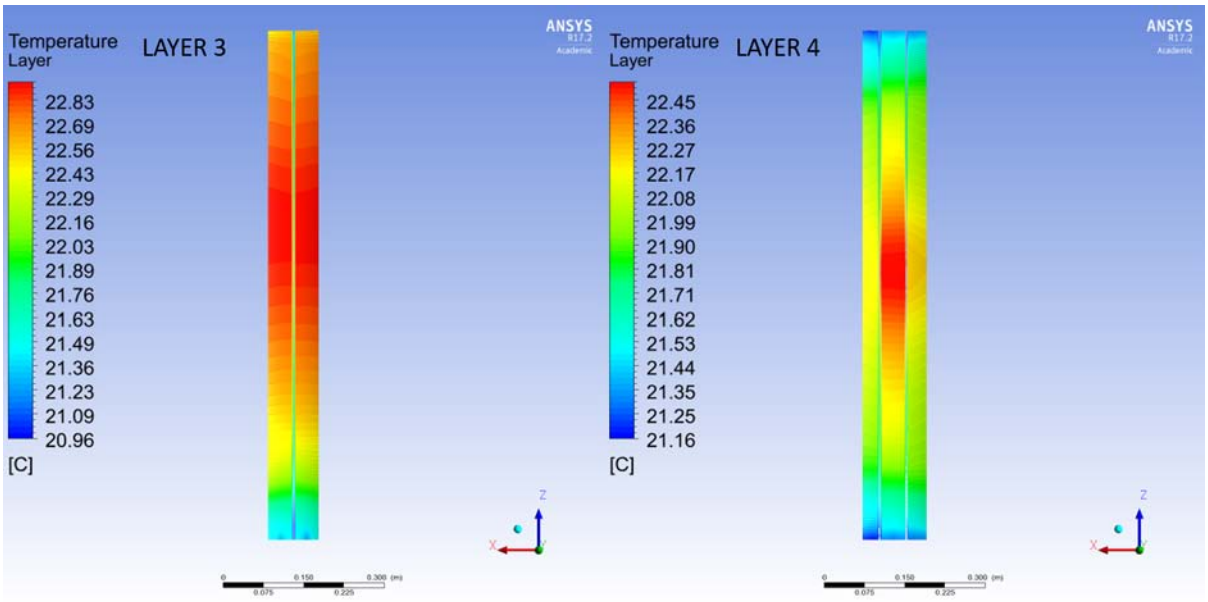

Figure 4.9: Temperature distribution along Layer 3 and Layer 4

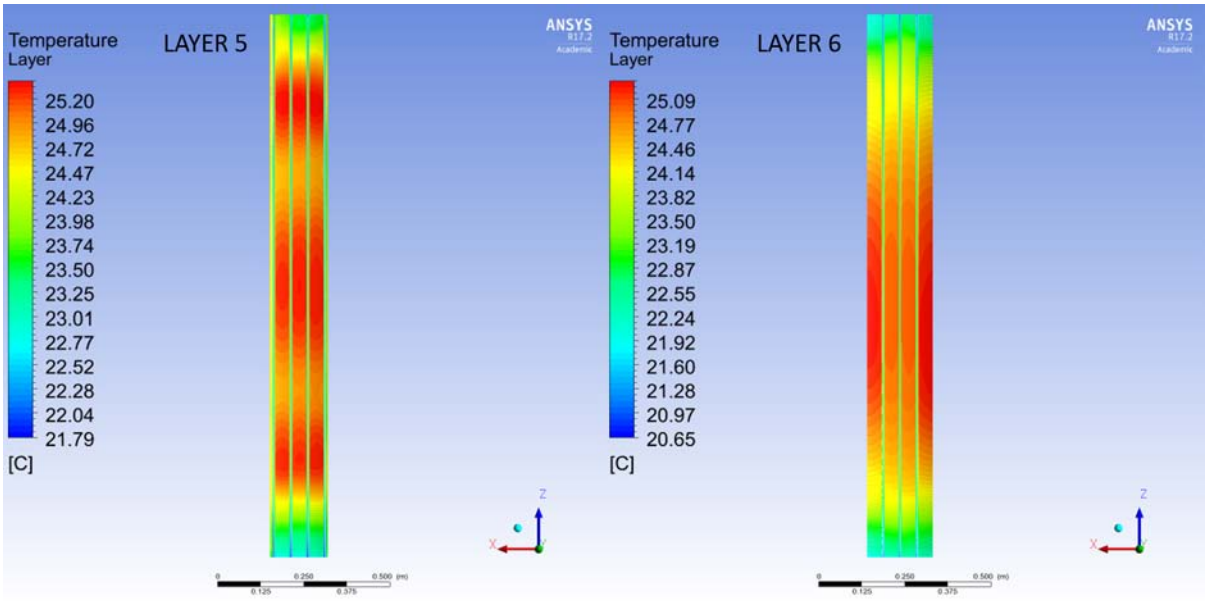

Figure 4.10: Temperature distribution along Layer 5 and Layer 6

4.2.5 Comparison between different air velocity inlets

As mentioned above, the air tends to be still in the middle of the barrel and the temperature rises. So, a way to reach the center of the barrel could be flushing air inside with a higher velocity inlet, to have more kinetic energy. However, as can be seen in Figure 4.11, also increasing the inlet velocity up to 3 m/s (bringing the mass flow inside the detector close to 90 m^3/h) doesn't help to have less non-uniformity in the temperature distribution. Shifting from 2 m/s to 3 m/s doesn't impact in a significant way the temperature distribution along Layers 3 and 4; regarding Layer 5 and 6, with a velocity of 3 m/s the maximum temperature value decreases respectively of 0.36 °C and 0.4 °C and the temperature gradient follows a similar trend (-0.2°C and -0.28 °C). This situation is related to the turbulent air flow established in near-nozzle zone of the barrel: the increased kinetic energy of the air at the nozzle is almost utterly dissipated in turbulent kinetic energy. It means that the air vortices near the nozzles don't let the air reaching the central part of the detector with a significant velocity. Furthermore, increasing the air mass flow in the detector means increasing the maximum velocity and it could lead to dangerous vibration problems.

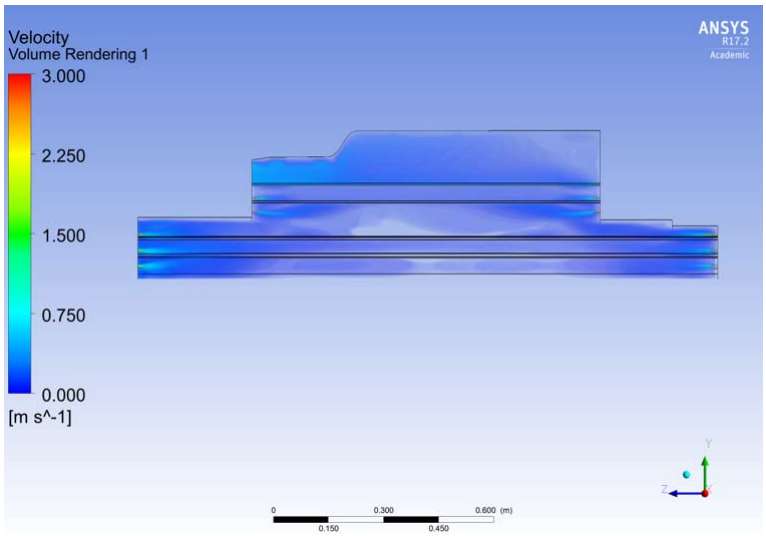

Figure 4.11: Volumetric velocity distribution with 3 m/s inlet

4.2.6 Assessment on air circulation effect on Barrel temperature

The aim of this simulation is to highlight the effect of the air circulation and to provide an overview of the hypothetical temperature distribution with air circulation

system inoperative. The boundary conditions for this analysis are:

- constant heat flux on the PB surfaces of the Outer Layers (20 W/m^2).
- constant heat flux on the PB surfaces of the Middle Layers (10 W/m^2).
- constant emissivity set at 0.7 for both PowerBus and ColdPlate and ColdPlate temperature fixed at 20°C.

The volumetric temperature distribution is shown in Figure 4.12.

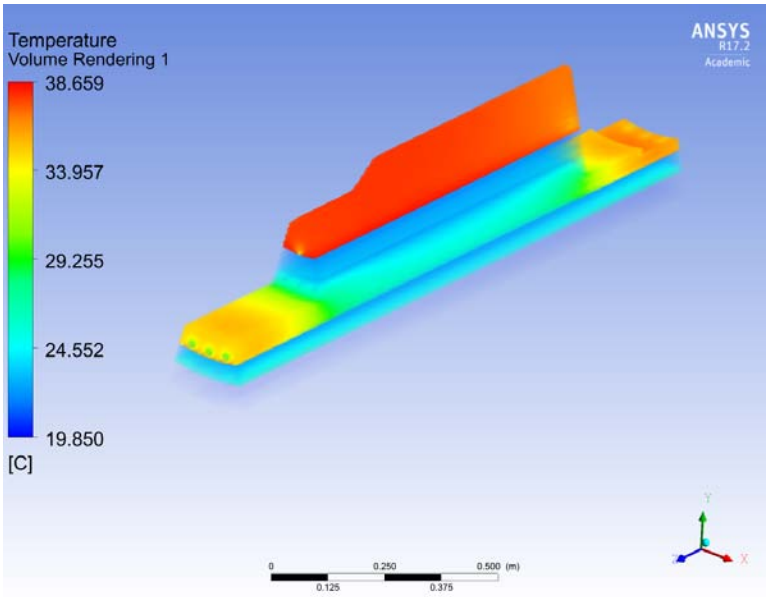

Figure 4.12: Volumetric temperature distribution without forced convection effects

As can be seen, the maximum temperature rises and reaches 38°C in the zones where the forced convection is the only way to carry away the heat dissipated by the PB. The plot is also useful to highlight the most critical zones in terms of barrel temperature; the top part of the barrel is hotter because there is no thermal radiation (there are no ColdPlates over the Layer 3) and without air convection the temperature rises fast. Others critical zones are located between the Outer Layer and the Middle Layer: in this region, there is the geometrical transition from 1500 mm length staves to 844 mm length staves. This means that the ColdPlate that exchange heat with the PowerBus is shorter (844 mm, on the bottom part of Layer 3) than the PowerBus itself (1500 mm, on the upper part of Layer 5). This is clearly shown in Figure 4.12, by referring the initial area of the volume over the Layer 5: the temperature is higher than in the central zone because all the heat is carried away by air convection. A closer look to Layer 3 and Layer 5 temperature with and without air convection is provided in Figure 4.13 and Figure 4.14:

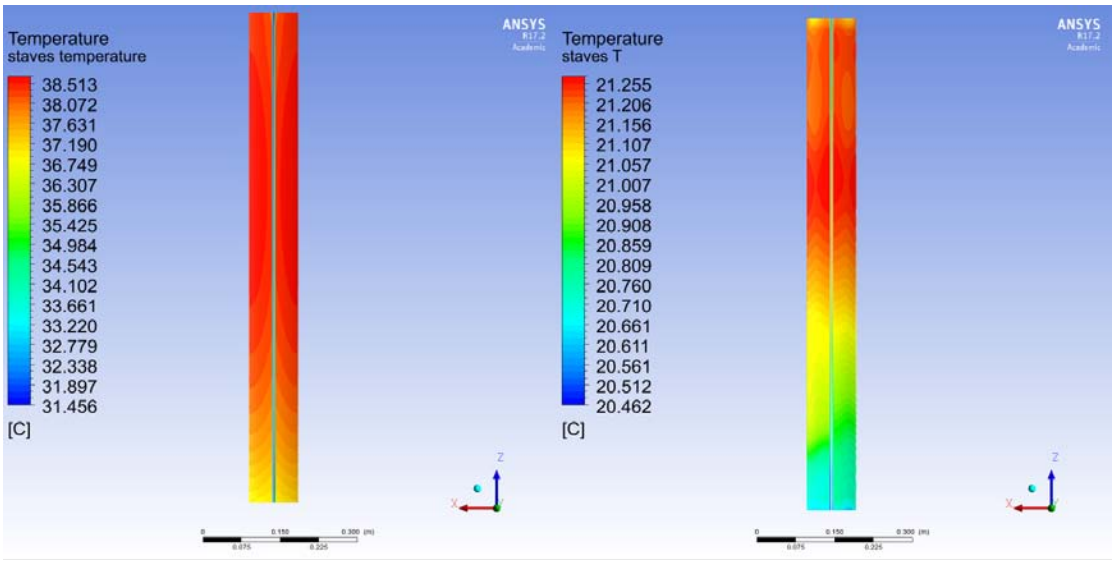

Figure 4.13: Temperature distribution without and with forced convection effects - Layers 3 and 4

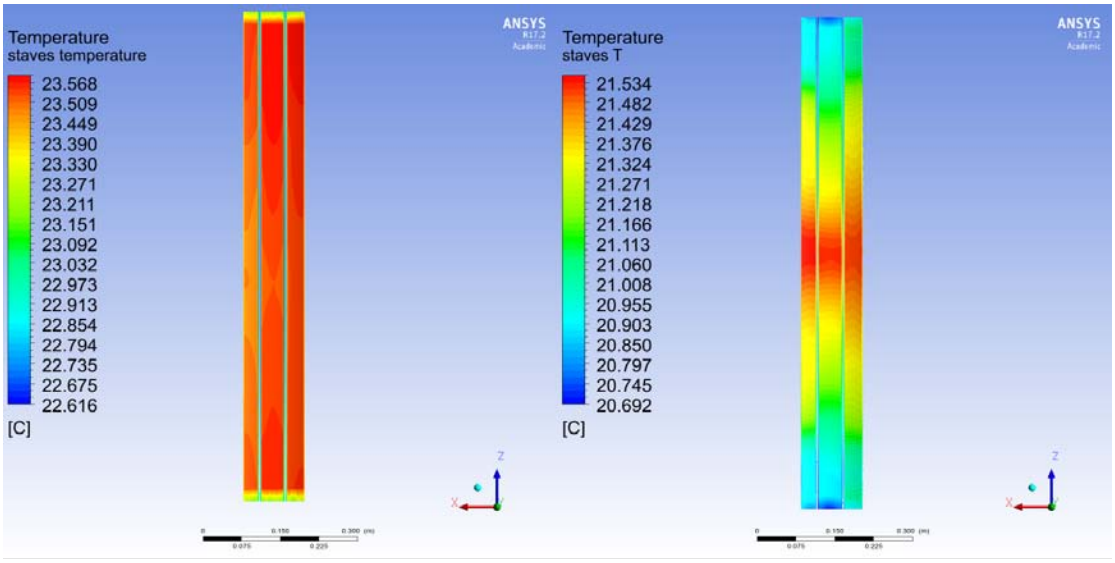

Figure 4.14: Temperature distribution without and with forced convection effects - Layers 5 and 6

4.3 Inner Barrel: Detector Side results

The Inner Barrel Staves are the part of the detector closer to the beams interaction point. The first row of staves lies at a distance of only 3 mm (considering the closer point) from the Beam Pipe surface (BP). For this reason and to not lose consistency the simulation has been developed considering the exact position of the staves in the layer, without simplification. Details on the mesh adopted (unstructured tetra mesh, about 7 million cells) can be found in Appendix D. As described above, the thermal boundary condition is related to the Beam Pipe heat dissipation for High Luminosity LHC and consist of a heat flux of 50 W/m^2 applied on the BP external surface. There are 15 air inlet nozzles, divided in two types: $\emptyset$5 mm nozzles that flush air from the Patch Panel (10) and $\emptyset$4 mm nozzles that flush the air in the region closer to the Beam Pipe (cf. Figure 3.10). The chosen velocity inlet for both the nozzles is 2.5 m/s (inlet air temperature set to 20 °C). The results are shown on Figure 4.15. The temperature is approximately well distributed in the staves region and presents two value peaks, one in the part before the stave region (in which the temperature is around 22°C) and one in the final part of the Barrel ((in which the temperature is around 32°C). This is related to the $\emptyset$4 mm nozzles position: the temperature is considerably low in the zone next to the inlet because the air velocity is high and thus the forced convection greater. In the final part, instead, the air velocity is lower than in the early part (around 0.6 m/s) and for this reason the temperature rises up.

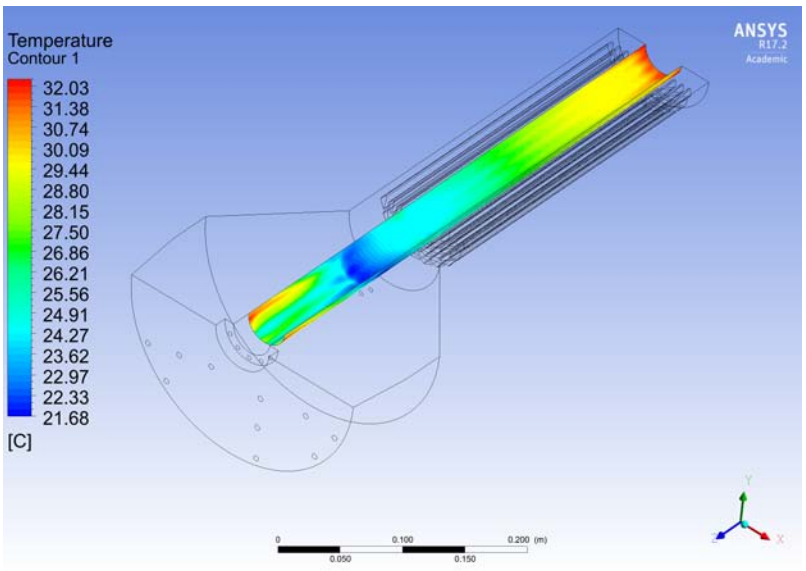

Figure 4.15: Temperature distribution along the Beam Pipe section, only forced convection

For the Inner Barrel, another simulation has been developed considering the staves as active parts in the heat transfer balance. The staves indeed are cooled down by the water cooling system and they are at a lower temperature than the air. The final equilibrium temperature is not a certain value because it is function of too many parameter, anyway it can be assumed that, thanks to the water cooling system support, they will not overcome the 22°C. In this case part of the heat emitted by the Beam Pipe will be transferred by thermal radiation to the cold - staves. Setting the emissivity values to 0.7 for both the surfaces (Beam Pipe and Staves), a maximum temperature of 28.18°C is reached in the out-of-staves zone, while 26.30°C is the final maximum temperature along the Beam Pipe (Figure 4.16).

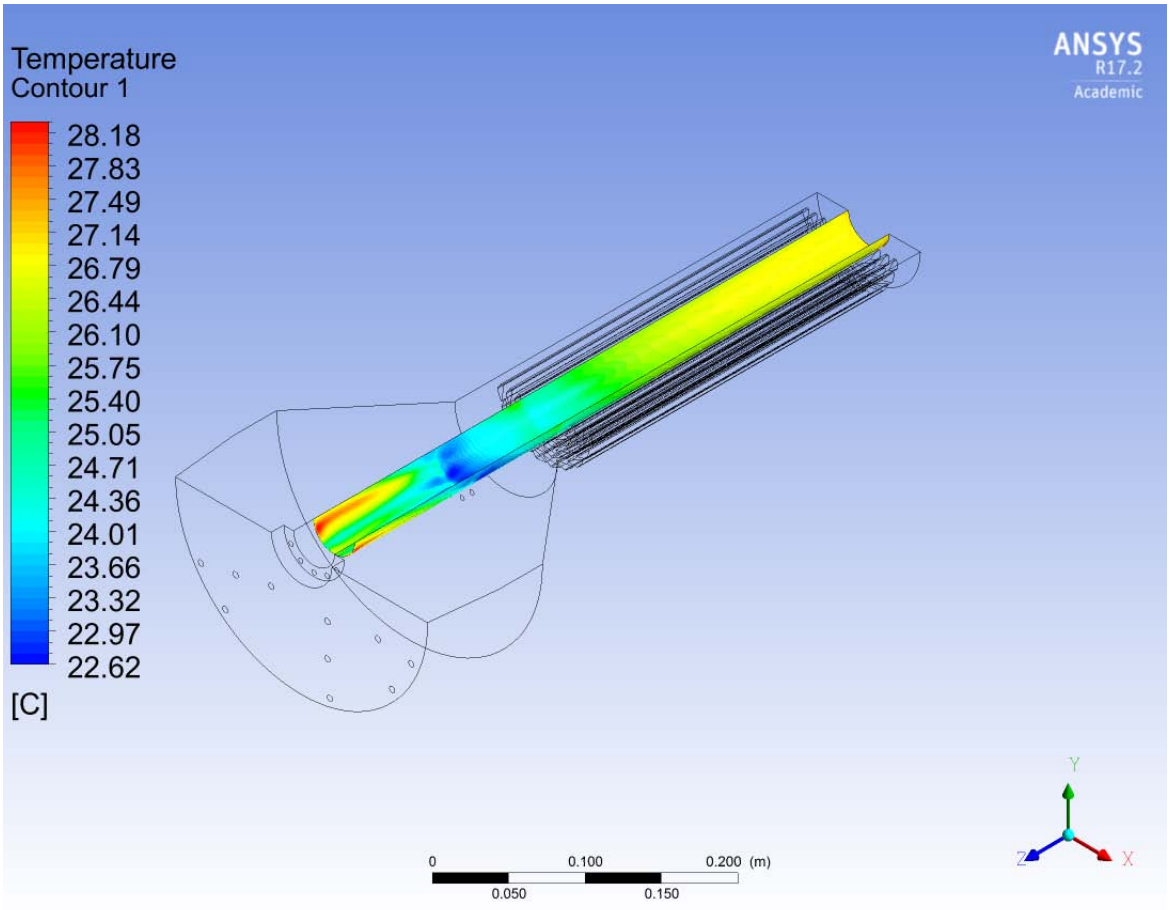

Figure 4.16: Temperature distribution along the Beam Pipe, forced convection and thermal radiation

4.4 Service Barrel results

The Service Barrel (SB) is the structure by which all the services are provided to the detector side. As stated above, the central part is accessible only by one side (A-side) so that all the cables and all the cooling pipes have to pass through the unique Service Barrel. The SB is divided in two parts, one for the Outer Barrel and one for the Inner Barrel (Figure 4.17). The air circulation system must provide a uniform distribution along the parts, removing the heat dissipated by the electrical cables of the OB (74 W) and of the IB (34 W). The air exiting the Detector is used to cool down the OB part because the air exit temperature is not high (considering 5 mm nozzles and 2 m/s of inlet velocity, the temperature gradient between inlet and exit detector is around 1.5°C). In addition, four rows of nozzles are used, flushing air from the End Wheels, as it seen above.

The critical situation related to the Service Barrels concerns with their length: it's not possible to flush the air only from the beginning of the Barrels themselves because, in this case it will not reach the end of the SB with an adequate velocity and so the temperature will rise up. Thus, to cool down the cables, intermediate air nozzles along the SB surface are needed. The challenge in this case is to optimize the values of inlet velocity and mass flow, considering that it is limited. In the case of the Outer Service Barrel a good compromise has been reached using 4 additional air inlets placed at the distance of about 500 mm each other. The air velocity has been set to 0.1 m/s to avoid vortices, in order to limit kinetic energy dissipation. As can be seen in Figure 4.18, with this kind of configuration a maximum temperature of 35.7°C is reached and it is an acceptable value (because the SB is far from the chips and thus higher temperatures don't influence the detector overall performances).

In the case of the Inner Service Barrel the surface on which the cables are placed is longer (it extends for 2.2 m of length) and there's no air available from

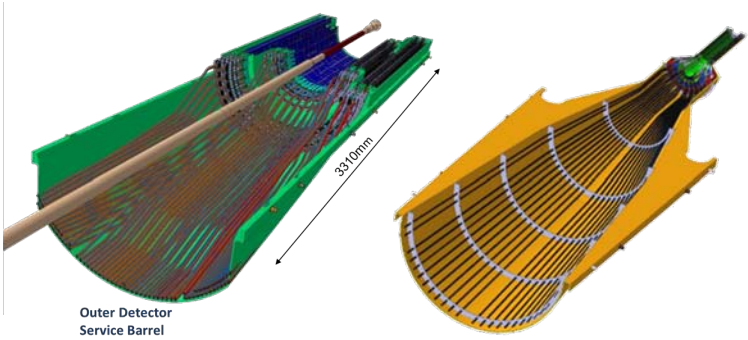

Figure 4.17: Outer Service Barrel and Inner Service Barrel [13]

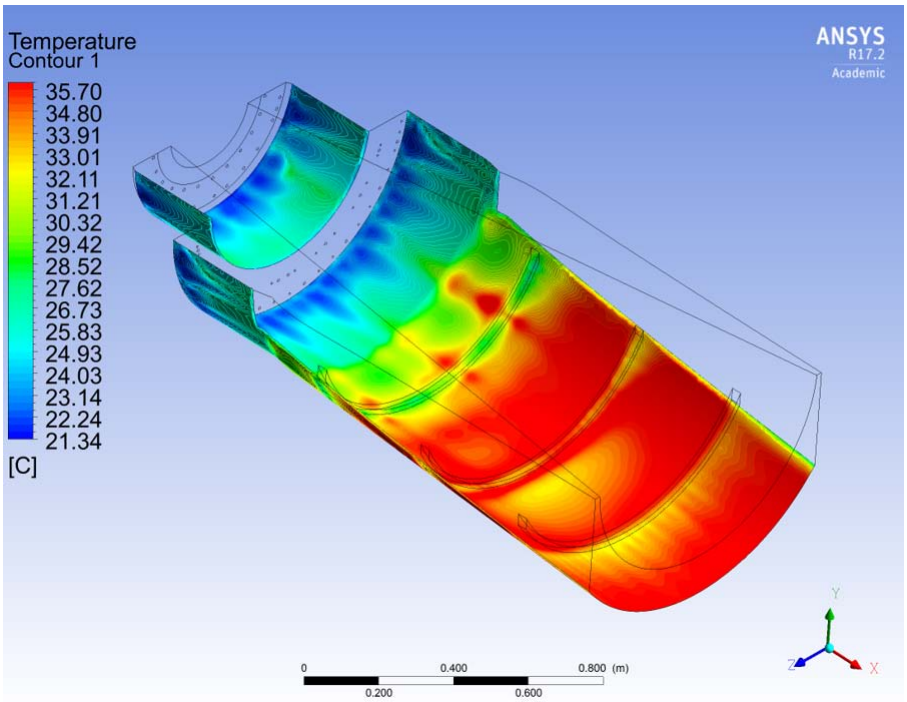

Figure 4.18: Outer Service Barrel temperature distribution

the detector side. In the initial configuration the air has to be flushed from the beginning of the Service Barrel, from the Patch Panel. However, after some simulations, it became clear that because of the SB length , two air inlet sections are needed. Using only one inlet is not possible because in this case the temperature rises to $40°C$. Splitting the mass flow in two inlets let the maximum temperature to not overcome the $34°C$, that is an acceptable value. To reach this temperature level a total mass flow of around 48 m^3/h is needed. The first inlet section flushes about 22 m^3/h at a velocity of 0.5 m/s while the second one (in the middle of the barrel) flushes about 26 m^3/h at the velocity of 0.3 m/s. Low levels of velocity has been chosen to limit the vortices near to the inlet zones, in order to avoid kinetic energy dissipation. These results are good by the point of view of the temperature, however the mass flow rate is too high. To lower it another air inlet has been placed at equal distance from the others. This measure let diminishing the total mass flow rate in the detector to 35 m^3/h maintaining the same maximum temperature levels (Figure 4.19). Furthermore, this solution leads to a decreasing of the inlets velocity to about 0.1 m/s.

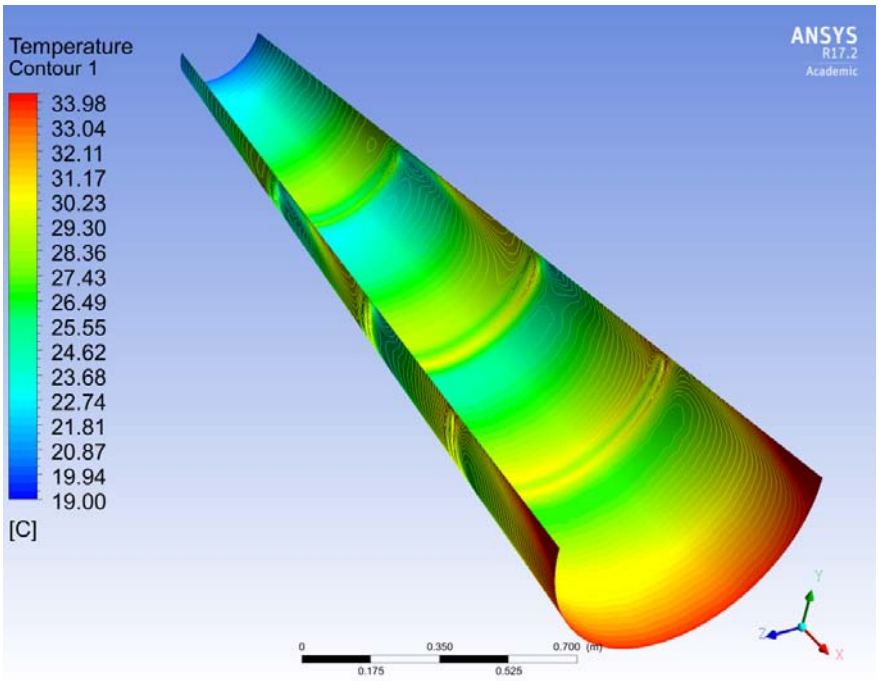

Figure 4.19: Inner Service Barrel Temperature Distribution

In general, for both Inner and Outer SB, the best solution to keep the temperature low and use the lower possible air flow rate is to multiply the inlet zones. However, adding inlets lead to another open question regarding the shape and the design of the inlets themselves. In the simulations, the air is flushed from the entire section (designed to obtain a specified mass flow rate a a certain velocity). Nonetheless, in the reality this solution could be non-approachable by the point of view of technical feasibility. For this reason, an initial simulation on the air flow behavior has been developed. The results, Figure 4.20, show that flushing the same flow rate of air with an open profile or 11 nozzles of ∅10 mm change totally the air behavior. With the open profile nozzle, the air is flushed at 0.1 m/s and it is distributed in an uniform way around all the Barrel. With the nozzles, instead, with an inlet velocity of 1.00 m/s there are vortices and the air is not well distributed. This brings to a non-uniformity of the temperature near the inlet zone. So, before optimizing the mass flow rate, a nozzle-design study has to be developed.

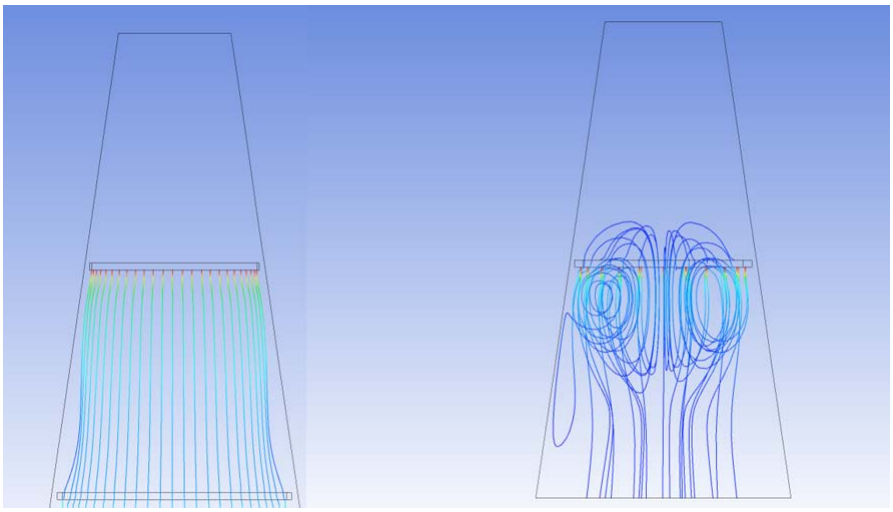

Figure 4.20: Comparison between inlet with a unique wide open nozzle and several circular small nozzles (same mass flow rate).

4.5 Assessment on Boundary Conditions parameters

4.5.1 Emissivity value effect on Stave temperature

A satisfactory esteem of the emissivity value of Kapton is difficult to obtain because it depends largely on the surface finishing of the structures and for this moment can't be measured experimentally. Literature values for the material range between the 0.7 and 0.8, so, to have a clear idea of the effect of PowerBus emissivity on staves temperature a dedicated simulation has been performed. Regarding ColdPlate emissivity, it is less difficult to esteem (simple carbon-fiber). The model has been built on three significant values of emissivity: the best scenario, PB emissivity $\epsilon = 0.9$, the worst scenario, PB emissivity $\epsilon = 0.1$ and the nominal scenario (0.7 with a 30% safety margin), PB emissivity $\epsilon = 0.5$. The others boundary conditions of the model are the following:

- nozzles of diameter 10 mm
- velocity inlet of 2.0 m/s
- ColdPlate Temperature fixed at 20°C.
- ColdPlate emissivity set at 0.7.

As can be seen in Figure 4.21, on the Layer 3 the thermal exchange due to radiation is limited (because there's no cold coldplate above) and so the emissivity variation on the PowerBus causes negligible temperature gradient (going from the better scenario, $\epsilon = 0.9$ to the worst one $\epsilon = 0.1$ the maximum temperature on the stave raises up of 0.4 °C).

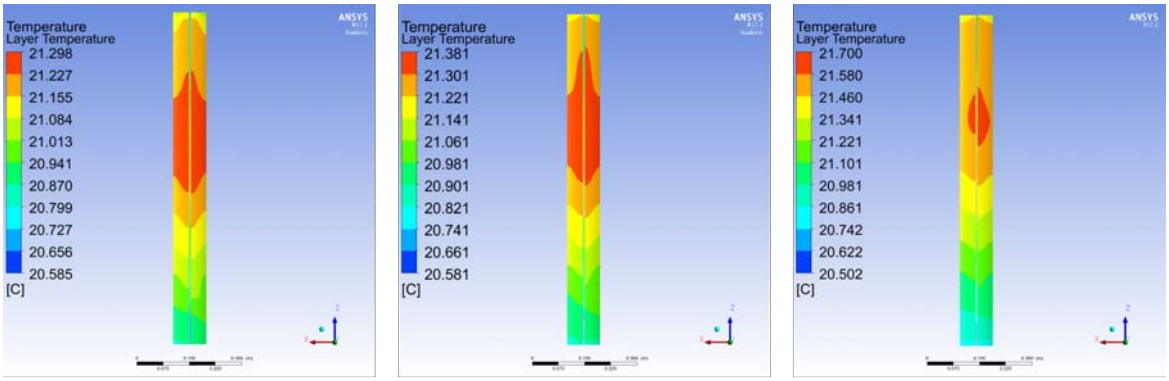

Figure 4.21: Temperature Contours on Layer 3 with the 3 different emissivity values

Figure 4.22 shows the situation on Layer 4: in this case part of the heat dissipated by the PowerBus is absorbed by the ColdPlate of Layer 3, directly above the PB of Layer 4. Consequently the effect of different emissivity value is greater and leads to an increase of the maximum temperature on the stave of 0.9 °C in the extreme conditions described above. Nonetheless considering the more likely scenario (emissivity that ranges from 0.5 to 0.1) the temperature difference is of 0.6°C, increase of temperature negligible (for the layer 4, as stated above, the threshold of maximum temperature is far from the estimated temperatures on the Layers).

The situation is clearly different regarding the Layer 5, as can be seen in Figure 4.23; in this zone of the detector the ratio between heat exchanged for radiation and heat exchanged for forced convection is higher (especially in the central part). This means that a variation on PB emissivity value increases in a considerable way the temperature on the staves. Considering the extreme values of emissivity, the maximum difference of temperature is of 2.8°C. Considering the nominal scenario, (range from 0.5 to 0.1) the maximum temperature difference is of around 2.0 °C and for the Layer 6 the situation is similar.

Anyway, considering the environmental detector condition, the quality of the surface finishing of the Kapton coverlay should not decay and the emissivity value should remain constant for the whole lifetime of the detector. Therefore, as shown

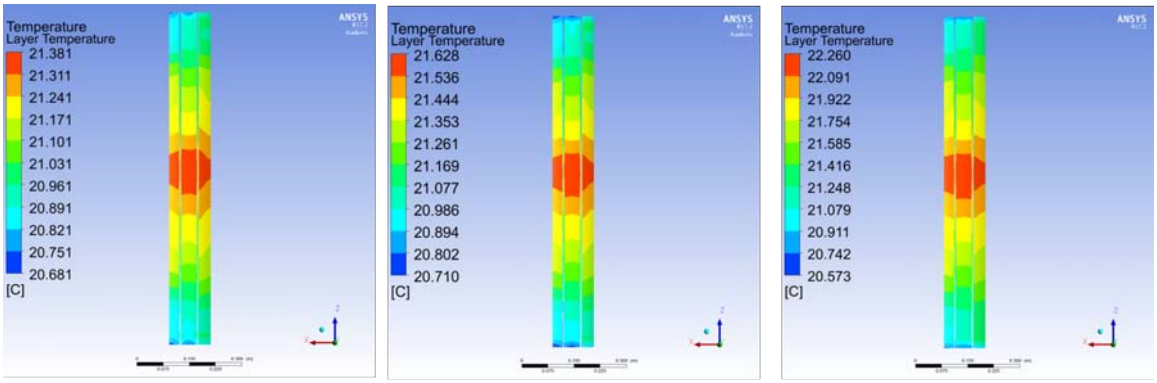

PB Epsilon = 0.9 PB Epsilon = 0.5 PB Epsilon = 0.1

Figure 4.22: Temperature Contours on Layer 4 with the 3 different emissivity values

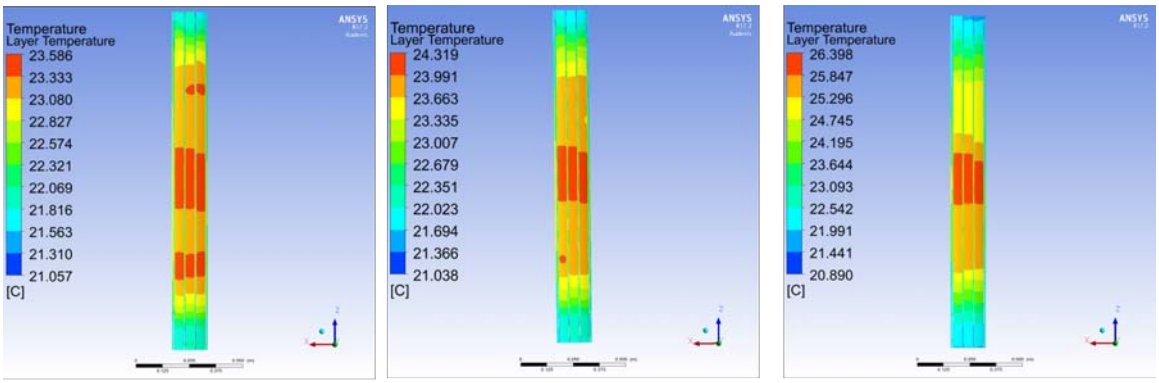

PB Epsilon = 0.9 PB Epsilon = 0.5 PB Epsilon = 0.1

Figure 4.23: Temperature Contours on Layer 5 with the 3 different emissivity values

in the section, choosing a value in the range between 0.6 and 0.8 will not influence in a considerable way the staves temperature.

4.5.2 Maximum air velocity in the critical point

As described above, using a simplified layer geometry, increases the grade of uncertainty regarding the maximum velocity inside the barrel. To investigate it, a detailed simulation using the real staves position has been carried out. To develop this analysis, a super-fine structured mesh has been created. With the minimum planar distance between half-staves of 0.8 mm, a cell sizing of 0.2 mm has been used, to be sure of catching the exact flow direction in this zone. Obviously, the geometry taken in account has been symmetric reduced and only one layer has been simulated with that precision (Layer 3, the most critical in terms of air velocity). Figure 4.24 shows the mesh obtained:

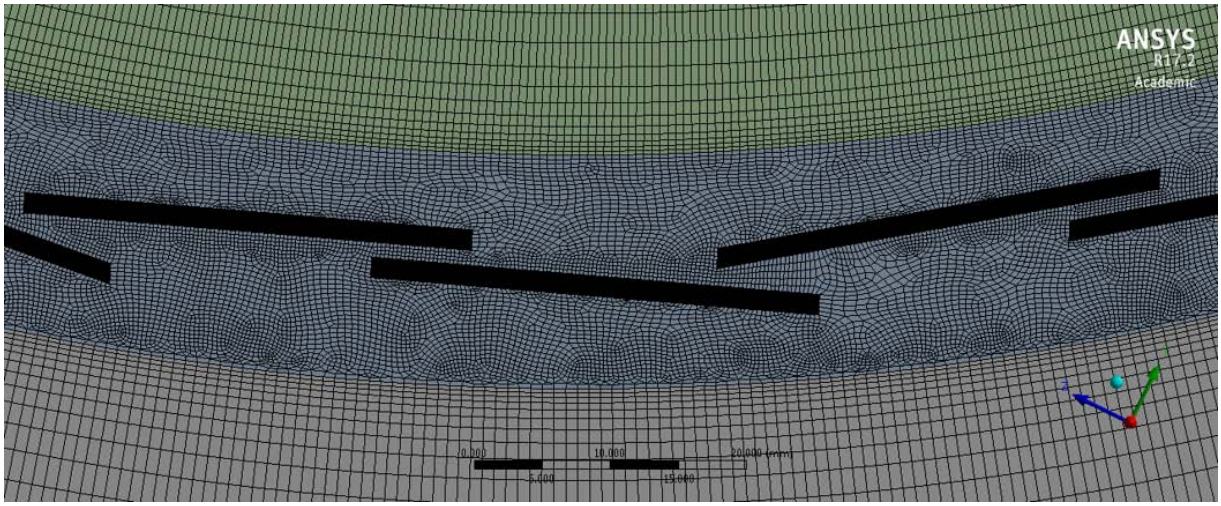

Figure 4.24: Hexaedral structured mesh used to find air trajectory between the half staves

The results are shown in Figure 4.25: as can be seen, the maximum velocity is 0.61 m/s, as expected a little higher than the velocity found with the simplified analysis (that was 0.48 m/s). This value is anyway below the threshold set to be acceptable (2 m/s). An interesting thing to observe is the air current that originates from the position of the half staves; as can be seen, the air-flow doesn't lap in the same way the upper and the lower half staves: over the upper half staves, in the right part, there are some vortices and the air seems to have a right-to-left flow direction. Therefore, probably the temperature on the lower half staves will be a bit lower (higher velocity and thus higher heat transfer convective coefficient).

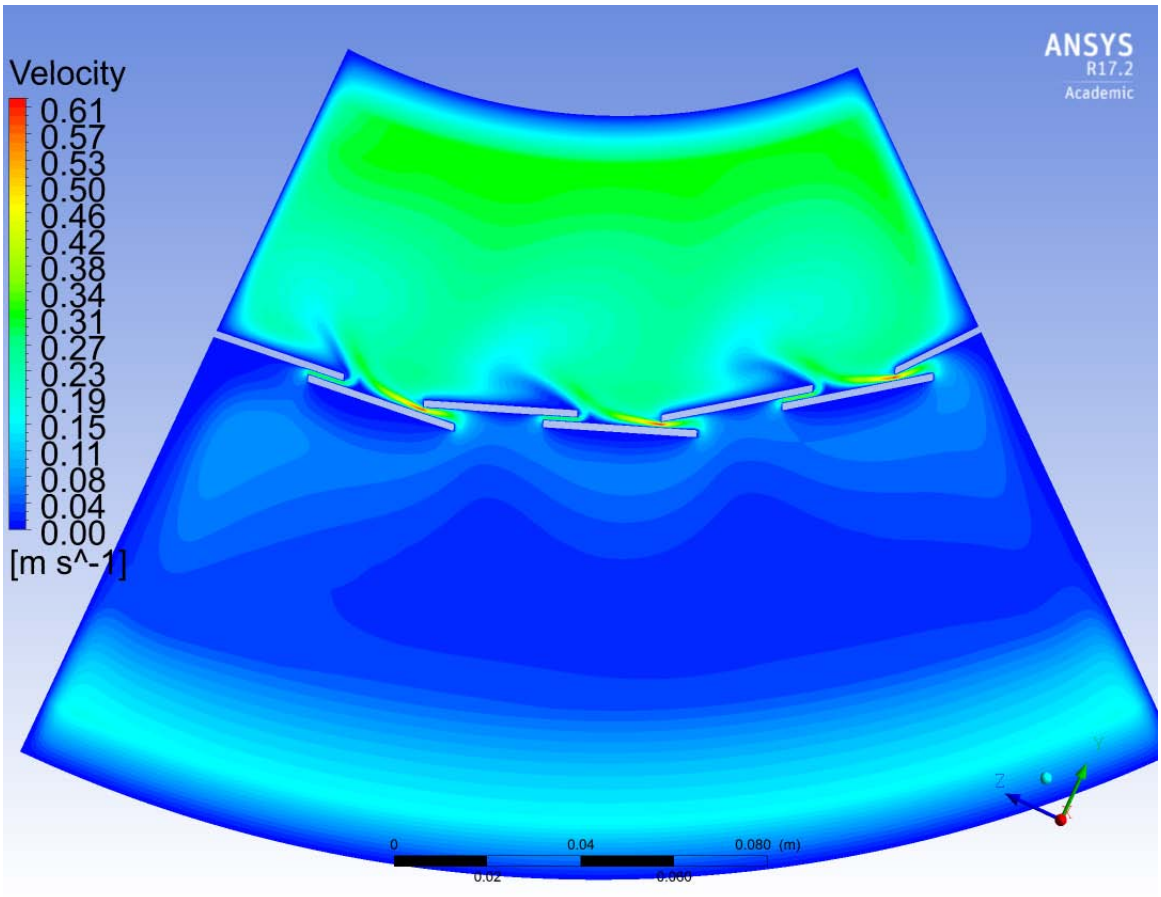

Figure 4.25: Velocity profile between the half staves of Layer 3

5 Conclusions

Final mass flow rate distribution

Overall Inner Tracking System

The final mass flow rate distribution among the components of the ITS is shown in Table 5.1. Starting from an expected configuration, the results of the simulations lead to a new mass flow rate distribution, especially taking in account of the SB needs. In particular, at the beginning, it was not expected a so high air flow rate along the SB, since the power dissipated in this zone is lower (34 W and 71 W) than the power dissipated inside the detector (180 W). Initially, a simple balance based on the first principle of thermodynamics suggested for the Inner Service Barrel (I-SB) an air flow of around 15 m^3/h. However, this value didn't take into account of the spatial distribution of the power (the surface of the I-SB is around 1.8 m^2) and the difficulties to reach with the same mass flow rate every region of this surface. So the effective mass flow rate needed for ISB is around 35 m^3/h) The same conclusion can be drawn for the Outer Service Barrel (O-SB).

Outer Barrel

Regarding the Outer Barrel, the final configuration adopted for the simulations is the one with ∅5 mm nozzles. The choice is justified by the poor advantages related to the ∅7 mm nozzles configuration: in this case, indeed, considering an inlet velocity of 2 m/s, the mass flow rate is doubled (about 120 $m3/h$) while the maximum temperature value decreases of only 0.4 °C, not enough to justify the higher cost of the pipes needed for the double mass flow rate. Furthermore, from the analysis it's clear that there's no reason to flush air at a velocity higher than 2 m/s: with higher velocity inlets, all the kinetic energy of the air is dissipated

Component	Mass Flow Rate [m³/h]
Inner Barrel - Detector	5
Inner Barrel - Service	35
Outer Barrel - Detector	60
Outer Barrel - Service	35
Envelope	25
MFT Detector	25
Lost in the environment	15
Total	200

Table 5.1: Final mass flow rate distribution

in turbulent vortices and it brings no benefits in terms of maximum temperature inside the Barrel. So, in the final configuration will be:

- 424 nozzles of 5 mm diameter
- velocity inlet of 2.0 m/s
- mass flow rate of $60 m^3/h$
- Inlet air temperature set to 20 °C and temperature gradient between inlet and outlet of 1.6°C.

Inner Barrel

In the Inner Barrel all the heat generated is carried out by the water cooling plant (the last experimental test on the IB PB shows that the heat dissipated by this component is negligible). So, the only thermal source inside the Barrel will be the Beam Pipe during High Luminosity LHC. The effective power to remove is low (about 1.5 W) and for this reason the mass flow needed is low; in the final configuration there will be:

- 10 nozzles of 5 mm diameter

- 5 nozzles of 4 mm diameter
- velocity inlet of 2.5 m/s
- mass flow rate of 2.3 m^3/h
- Inlet air temperature set to 20 °C and temperature gradient between inlet and outlet of 1.63°C.

Service Barrel

The Service Barrel represents an exception in the ITS cooling configuration because in this case all the heat dissipated by the components has to be removed by the air (there isn't a water cooling dedicated plant or a constant low temperature surface for thermal radiation). As explained in the previous chapter, the inlet points must be distributed inside the Barrel. The mass flow rate of 35 m^3/h for the I-SB and 35 m^3/h for the O-SB (in addition to the 60 m^3/h coming from the detector) are a good compromise and doesn't let the temperature rising to dangerous values. Another consideration to do is that part of the services running along the Service Barrel is composed by the water cooling pipes; the temperature of the water in the pipes will be sensibly lower than the air temperature and, probably, part of the heat dissipated by the electrical cables will be absorbed by the water itself. Therefore, the temperature shown in the previous chapter are the worst scenario. In the real situation, the temperature will be lower.

Overview on the maximum temperatures and the temperature gradients

Table 5.2 shows the final temperatures inside the ITS. As can be seen, in the Detector Side the maximum temperature is lower than in the Service Side in order to maintain the optimal operating conditions for the electronic components. In this zone, the temperature gradient is low and an acceptable temperature uniformity has been achieved.

Component	Mass flow rate [m^3/h]	Dissipated Power [W]	Maximum Temperature in the Barrel [°C]	Maximum Temperature Gradient in the Barrel [°C]	Air ΔT (inlet at 20°C) [°C]	Maximum Velocity in the detector [m/s]
Inner Barrel - Detector	5	1.5	28.18	5.58	2.83	0.71*
Outer Barrel - Detector	60	182	25.39	5.54	1.60	0.65*
Inner Barrel - Service	35	34	34.67**	15.67	3.2	0.3
Outer Barrel - Service	35***	71	35.70**	14.36	/	2.00

*excluding nozzles inlet velocity
**worst scenario
*** 25 m^3/h from the additional inlets and 10 m^3/h from the End Wheels. Other 60 m^3/h comes from the OB Detector. So, the total air flow over the Outer Service Barrel will be of 95 10 m^3/h

Table 5.2: Final temperature values inside the Barrels

Regarding the Outer Barrel Layers temperature (shown in Table 5.3), as already described a considerable part of the heat is carried away for thermal radiation between the PowerBus and the ColdPlate. This has to be considered in the design of the water cooling system of the stave (embedded in the CP): it could be necessary to adjust the water mass flow rate or the water inlet temperature.

The same occurs in the Inner Barrel: the maximum temperature obtained and reported in Table 5.2 is the one that takes into account of the radiative heat transfer between Beam Pipe and staves with the staves at a constant temperature (22 °C). Considering the other studied scenario (heat transfer only via forced convection) means to assume that the staves are at higher temperature (close to the BP temperature) and, thus, to assume the water cooling system doesn't work properly.

Finally, considering the SB, some design choices have to be made. As mentioned above, all the cooling system pipes will pass through it. If the cooling pipes will be insulated, there will not be heat transfer between electrical cables and the pipes. In this scenario, the maximum temperature will be the one shown in Figure 4.19 and 4.20. With not insulated cooling pipes, part of the heat dissipated by the cables will heat up the water. In this case, the water will reach the Patch Panel and the End-Wheels at a slightly higher temperature .

Layers*	Maximum temperature on the stave [°C]	Temperature gradient along the stave [°C]	Total Power dissipated by the PB [W]	Power transferred via thermal radiation [W]	% of power transferred via thermal radiation
Layer 3	22.83	1.87	12	/	/
Layer 4	22.45	1.29	15	7.2	48%
Layer 5	25.20	3.41	72	34.6	48%
Layer 6	25.09	4.44	83	53.9	65%
		TOTAL	182	95.7	53% of the total

* For Layers 0, 1 and 2 (Inner Barrel) the power dissipated by the Power Bus is negligible

Table 5.3: Layer power and temperature distribution

Next developments

Some other evaluations are needed to fully characterize the ITS air circulation. First, a complete map of the air trajectory in the transition zone between the Inner Barrel and the Outer Barrel to highlight the exact air flow direction. Another further development is related to the Service Barrels: at that time there isn't yet a design of the nozzles that flush air. A study should be developed to identify the optimal configuration of these components (shape, dimension, number). Other useful simulations could be related to the rectangular air ducts that bring air from the A-side to the C-side, to assess the maximum air velocity. Finally, close to the ITS, there's another detector, MFT (Muon Forward Tracker). Since they share the same air circulation volume, an integrated simulation should be developed, taking in account also of the MFT needs (Figure 5.1).

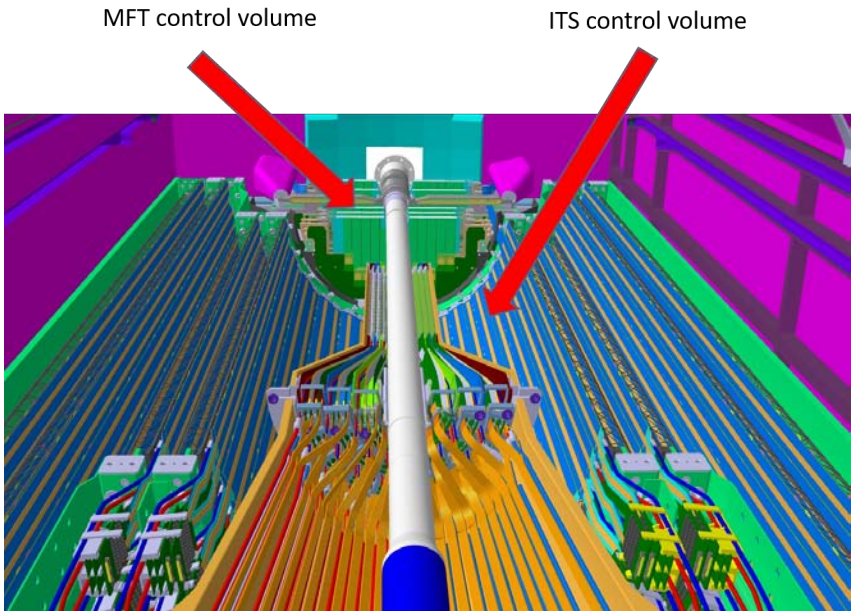

Figure 5.1: ITS and MFT control volumes - section [12]

Appendix A: Ansys Fluent mathematical models

All the appendix refers and is based on the Ansys Academic Research documentation, Release 17.2. [27]

A.1 Mass and Momentum conservation equations

The general equation for conservation of mass, or continuity equation, can be written as follows:

$$\frac{\partial \rho}{\partial t} + \nabla \cdot (\rho \vec{v}) = S_m$$

where ρ is the fluid density, $\vec{v}$ is the vector of the velocity of the fluid and the source term S_m is the mass added to the continuous phase from the dispersed second phase or any user-defined function.

Regarding the air simulation, in this equation a first assumption is defined: considering the expected situation (small temperature gradient inside the barrels) the air supposed to be incompressible and in a single phase; so, the continuity equation for the model is:

$$\nabla \cdot (\rho \vec{v}) = 0$$

Conservation of momentum in an inertial reference frame is described by the equation:

$$\frac{\partial \rho}{\partial t}(\rho \vec{v}) + \nabla \cdot ((\rho \vec{v} \vec{v}) = -\nabla p + \nabla \cdot (\overline{\overline{\tau}}) + \rho \vec{g} + \vec{F}$$

where p is the static pressure, $\overline{\overline{\tau}}$ is the stress tensor and $\rho \vec{g}$ and $\vec{F}$ are the gravitational body force and external body force. The stress tensor is given by:

$$\overline{\overline{\tau}} = \mu\Big[(\nabla\vec{v} + \nabla\vec{v}^T) - \frac{2}{3}\nabla\cdot\vec{v}I\Big]$$

where μ is the molecular viscosity, I is the unit tensor and the second term on the right side is the effect of volume dilation.

A.2 Turbulence Modeling

Turbulent flows are inherently unsteady, three dimensional and irregular. A broad range of time and length scales exist in this kind of flows, anyway in general they are governed by the Navier-Stokes equations. The need to resolve all scales from the dissipative (Kolmogorov) scales to the mean flows scales makes direct simulation too expensive to be feasible for industrial applications. Reynolds Averaging is one of the approaches used to eliminate small scales. The application of this approach leads to the Reynolds Averaged Navier-Stokes equations (RANS). The Reynolds stress terms in the RANS equation require modeling in order to obtained a closed system of equations (closure problem). Two branches of RANS modeling are Eddy Viscosity Models (EVM) and Reynolds stress models (RSM). The set of equations used to solve the simulations presented are the so-called $k-\epsilon model$ (RANS RSM). In this kind of model two equations and two transported variables are calculated; the first transported variable determines the energy in the turbulence and it is called turbulent kinetic energy (k). The second transported variable is the turbulent dissipation (ϵ) which determines the rate of dissipation of the turbulent kinetic energy. The two equations are the following:

$$\rho\frac{Dk}{Dt} = \frac{\partial}{\partial x_j}\Big[(\mu + \frac{\mu_t}{\sigma_k})\frac{\partial k}{\partial x_j}\Big] + \mu_t S^2 - \rho\epsilon$$

$$\rho\frac{D\epsilon}{Dt} = \frac{\partial}{\partial x_j}\Big[(\mu + \frac{\mu_t}{\sigma_\epsilon})\frac{\partial \epsilon}{\partial x_j}\Big] + \frac{\epsilon}{k}(C1_\epsilon\mu_t S^2 - \rho C2_\epsilon\epsilon)$$

In particular, in the model has been adopted the *Realizable* version of the equations with *Enhnanced Wall Treatment* to solve the Boundary Layer.

A.3 Heat Tranfer equations

A.3.1 Forced convection

Ansys Fluent solves the energy equation in the following form:

$$\frac{\partial}{\partial t}(\rho E) + \nabla(\overline{v}(\rho E + p)) = \nabla\Big(k_{eff}\nabla T - \sum_{j=1}^{N} h_j \overline{J_j} + (\overline{\overline{\tau_{eff}}\overline{v}})\Big) + S_h$$

where k_eff is the effective conductivity ($k + k_t$, where k_t is the turbulent thermal conductivity, defined according to the turbulence model used) and $\overline{J_j}$ is the diffusion flux of species j (not considered in the simulation). The first three terms on the right-hand side of the equation represent energy transfer due to conduction, species diffusion and viscous dissipation, respectively. S_h includes volumetric heat sources (included radiation terms). The term E is related to enthalpy:

$$E = h - \frac{p}{\rho} + \frac{v^2}{2}$$

where sensible enthalpy h is defined for incompressible flows as

$$h = \sum\nolimits_j Y_j h_j + \frac{p}{\rho}$$

where Y_i is the mass fraction of the species j and

$$h_j = \int_T^{T_{ref}} C_{p,j} dT$$

. The value used for T_{ref} is 298.15 K.

A.3.2 Thermal Radiation: the Surface to Surface (S2S) Model

Citing vastly the *ANSYS theory guide: Surface to Surface (S2S) Radiation Model heory - ANSYS Academic Research, Release 17.2*

To model thermal radiation the Ansys Fluent SurfaceToSurface (S2S) model has been chosen. It can be used to account for the radiation exchange in an enclosure of gray-diffuse surfaces. The energy exchanged between the two surfaces depends in part on their size, separation distance and orientation. These parameters are accounted for by a geometric function called View Factor. The main assumption of the S2S model is that any absorption, emission or scattering of radiation can be ignored.

Gray-Diffuse Radiation

The first hypothesis on which S2S model is based is that the radiating surfaces are gray and diffuse. It means that emissivity and absorptivity are independent of

the wavelenght. Also, by Kirchoff's law the emissivity is equal to the absorptivity ($\epsilon = \alpha$). Furthermore, for a diffuse surface, the reflectivity is independent of the outgoing or incoming directions. Accordingly to the gray-body model, if a certain amount of radiant energy (E) is incident on a surface, a fraction (ρE) is reflected, a fraction (αE) is absorbed and a fraction (τE) is transmitted. The surfaces in use are opaque to thermal radiation (in the infra-red spectrum) and thus the transmissivity can be neglected. From the conservation of energy it follows that $\alpha + \rho = 1$ since $\alpha = \epsilon$ and $\rho = 1 - \epsilon$.

The S2S model equations

As a consequence of the gray-body model, the energy flux leaving the surface is composed of directly emitted and reflected energy. The reflected energy flux is dependent on the incident energy flux from the surroundings, express also in terms of energy flux leaving all other surfaces. In this case, the energy leaving the surface k is

$$q_{out,k} = \epsilon_k \sigma T_k^4 + \rho_k q_{in,k}$$

where $q_{out,k}$ is the energy flux leaving the surface, ϵ_k is the emissivity, σ the Stefan-Boltzmann constant and $q_{in,k}$ is the energy flux incident on the surface from the surroundings.

The amount of incident energy upon a surface from the other surface is a direct function of the above-cited view factor F_{jk}. It indicates the fraction of energy leaving j that is incident on the surface k. The incident energy flux $q_{in,k}$ can be expressed in terms of the energy flux leaving all the other surfaces as

$$A_k q_{in,k} = \sum_{j=1}^{N} A_j q_{out,j} F_{j,k}$$

where A_k is the area of the surface k. For N surfaces, using the view factor reciprocity relationship gives

$$A_j F_{jk} = A_k F_{kj} for j = 1, 2, 3, ...N$$

it leads to

$$q_{in,k} = \sum_{j=1}^{N} F_{kj} q_{out,j}$$

Therefore,

$$q_{out,k} = \epsilon_k \sigma {T_k}^4 + \rho \sum_{j=1}^{N} F_{kj} q_{out,j}$$

which can be written as

$$J_k = E_k + \rho_k \sum_{j=1}^{N} F_{kj} J_i$$

where J_k represents the energy that is given off (Radiosity) of surface k and E_k represents the emissive power of surface k. This represent N equations, can be cast into a matrix form as

$$KJ = E$$

where K is an NxN matrix, J is the radiosity vector and E is the emissive power vector.

The view factor between two finite surfaces i and j is given by

$$F_{ij} = \frac{1}{A_i} \iint_A \frac{cos\theta_i cos\theta_j}{\pi r^2} \delta_{ij} \, dA_i \, dA_j$$

where $\delta_{i,j}$ is determined by the visibility of dA_j to dA_i. If $\delta_{i,j} = 1$, dA_j is visible only to dA_i and 0 otherwise.

The considered view factors can be seen in Table A.1.

From coldplate3 to:		From coldplate4 to:		From coldplate5 to:		From coldplate6 to:	
	Viewfactor		Viewfactor		Viewfactor		Viewfacto
coldplate3	0	coldplate3	0	coldplate3	0	coldplate3	0
coldplate4	0	coldplate4	0	coldplate4	0	coldplate4	0
coldplate5	0	coldplate5	0	coldplate5	0	coldplate5	0
coldplate6	0	coldplate6	0	coldplate6	0	coldplate6	0
inlets	0.000324	inlets	0.000011	inlets	0.00023	inlets	0.000194
inlets_direct_aside	0.000009	inlets_direct_aside	0.000182	inlets_direct_aside	0	inlets_direct_aside	0
inlets_direct_cside	0.000012	inlets_direct_cside	0.000188	inlets_direct_cside	0	inlets_direct_cside	0
outlet	0	outlet	0	outlet	0	outlet	0
stave3	0	stave3	0	stave3	0	stave3	0
stave4	0.910349	stave4	0	stave4	0	stave4	0
stave5	0.036338	stave5	0.884522	stave5	0	stave5	0
staves6	0.002282	staves6	0.060611	staves6	0.927937	staves6	0
wall-part-part1	0.050685	wall-part-part1	0.054486	wall-part-part1	0.071833	wall-part-part1	0.999806
From inlets to:		From inlets_direct_a	side to:	From inlets_direct_c	side to:	From outlet to:	
	Viewfactor		Viewfactor		Viewfactor		Viewfacto
coldplate3	0.050593	coldplate3	0.010914	coldplate3	0.009199	coldplate3	0
coldplate4	0.001076	coldplate4	0.344357	coldplate4	0.346335	coldplate4	0
coldplate5	0.089286	coldplate5	0	coldplate5	0	coldplate5	0
coldplate6	0.098404	coldplate6	0	coldplate6	0	coldplate6	0
inlets	0	inlets	0	inlets	0	inlets	0.000082
inlets_direct_aside	0	inlets_direct_aside	0	inlets_direct_aside	0	inlets_direct_aside	0
inlets_direct_cside	0	inlets_direct_cside	0	inlets_direct_cside	0	inlets_direct_cside	0
outlet	0.000748	outlet	0	outlet	0	outlet	0
stave3	0.056746	stave3	0	stave3	0.000233	stave3	0.69675
stave4	0.106423	stave4	0.00058	stave4	0.000811	stave4	0.012621
stave5	0.143571	stave5	0.58742	stave5	0.58154	stave5	0.000419
staves6	0.165672	staves6	0.025745	staves6	0.03452	staves6	0
wall-part-part1	0.287482	wall-part-part1	0.030984	wall-part-part1	0.027362	wall-part-part1	0.290128
From stave3 to:		From stave4 to:		From stave5 to:		From staves6 to:	
	Viewfactor		Viewfactor		Viewfactor		Viewfacto
coldplate3	0	coldplate3	0.741286	coldplate3	0.012667	coldplate3	0.000619
coldplate4	0	coldplate4	0	coldplate4	0.387989	coldplate4	0.022897
coldplate5	0	coldplate5	0	coldplate5	0	coldplate5	0.786502
coldplate6	0	coldplate6	0	coldplate6	0	coldplate6	0
inlets	0.000365	inlets	0.000657	inlets	0.000376	inlets	0.000335
inlets_direct_aside	0	inlets_direct_aside	0	inlets_direct_aside	0.00011	inlets_direct_aside	0.000005
inlets_direct_cside	0	inlets_direct_cside	0.000001	inlets_direct_cside	0.000112	inlets_direct_cside	0.000009
outlet	0.040502	outlet	0.000601	outlet	0.000011	outlet	0
stave3	0.540885	stave3	0.007202	stave3	0.000218	stave3	0
stave4	0.008811	stave4	0.168556	stave4	0.000904	stave4	0.00004
stave5	0.000565	stave5	0.002039	stave5	0.187492	stave5	0.004186
staves6	0	staves6	0.000111	staves6	0.004861	staves6	0.10852
wall-part-part1	0.408872	wall-part-part1	0.079548	wall-part-part1	0.405259	wall-part-part1	0.076887
From wall-part-part1	to:						
	Viewfactor						
coldplate3	0.007512						
coldplate4	0.009901						
coldplate5	0.029793						
coldplate6	0.490502						
inlets	0.000291						
inlets_direct_aside	0.000003						
inlets_direct_cside	0.000003						
outlet	0.002543						
stave3	0.061586						
stave4	0.014601						
stave5	0.169567						
staves6	0.037321						
wall-part-part1	0.176378						

Table A.1: Outer Barrel - view factors

B

Bibliography

[1] Marcel Proust (translated by C. K. Moncrief). Remembrance of things past or in search of lost time, volume 5 - the prisoner, [1923].

[2] CERN collaboration. http://home.cern/topics/large-hadron-collider, [accessed dec. 2016].

[3] Wikipedia. https://en.wikipedia.org/wiki/cern, [accessed dec. 2016].

[4] CERN collaboration. https://home.cern/about, [accessed dec. 2016].

[5] ALICE collaboration. Alice phyiscs, available online at http://aliceinfo.cern.ch/public/en/chapter1, [accessed dec. 2016].

[6] ALICE collaboration. Free quarks and gluons, available online at http://aliceinfo.cern.ch/public/en/chapter2, [accessed dec. 2016].

[7] ALICE collaboration. Alice technical design report of the upgrade of the inner tracking system (its). Technical report, CERN-LHCC-2013-024, ALICE TDR 017, 2013.

[8] ALICE collaboration. Detectors of the alice experiment, available online at http://aliceinfo.cern.ch/public/en/chapter2/page3-subdetectors-en.html, [accessed dec. 2016].

[9] G Dellacasa et al. Alice technical design report of the inner tracking system (its). Technical report, CERN-LHCC-99-12, ALICE TDR 4, 1999.

[10] Cristina Terrevoli (Università di Bari and INFN) on behalf of the ALICE ITS Upgrade Collaboration. Studies for an upgrade of the alice inner tracking system. Technical report, CERN- ALICE ITS Upgrade Collaboration, 2012.

[11] Corrado Gargiulo on behalf of the ALICE ITS Upgrade Collaboration. Alice ob space frame and cold plate, stave engineering design review (edr). Technical report, CERN- ALICE ITS Upgrade Collaboration, May 2016.

[12] Corrado Gargiulo on behalf of the ALICE ITS Upgrade Collaboration. Alice inner barrel detector mechanics, detector barrel mechanics production readiness review (prr). Technical report, CERN- ALICE ITS Upgrade Collaboration, November 2016.

[13] Corrado Gargiulo on behalf of the ALICE ITS Upgrade Collaboration. Alice service barrel detector mechanics, detector barrel mechanics engineering design review (edr). Technical report, CERN- ALICE ITS Upgrade Collaboration, December 2016.

[14] Elisa Laudi on behalf of the ALICE ITS Upgrade Collaboration. Alice detector layout and stave, cooling system production readiness review (prr). Technical report, CERN- ALICE ITS Upgrade Collaboration, December 2016.

[15] Henry David Thoreau. Walden or life in the woods, chapter 2 - where i lived and what i lived for, [1854].

[16] ALICE ITS Upgrade Collaboration. Alice detector, its upgrade power bus and bias bus design. Technical report, CERN- ALICE ITS Upgrade Collaboration, December 2016.

[17] ALICE ITS Upgrade Collaboration. Alice detector. its upgrade power system status, plenary meeting. Technical report, CERN- ALICE ITS Upgrade Collaboration, January 2017.

[18] CERN collaboration. http://hilumilhc.web.cern.ch/, [accessed dec. 2016].

[19] ANSYS inc. Ansys fluent intro, 15.0 release, lecture2: Introduction to cfd methodology, slide 7, how does cfd works?, [2013].

[20] Frank P. Incropera-David P. Dewitt-Theodore L. Bergman-Adrienne S. Lavine. *Principle of Heat and Mass Transfer*. John Wiley and Sons, Inc., 2013.

[21] B.S in T.F. Irvine Petukhov and J.P. Hartnett. *Advances in Heat Transfers*. Academic Press, New York, 1970.

[22] V. Gnielinski. New equations for heat and mass transfer in turbulent pipe flow and channel flow. *International Chemical Engineering*, (16):359–368, 1976.

[23] ANSYS inc. Ansys fluent intro, 15.0 release, lecture8: Modelling heat transfer, slide 7, modelling heat transfers in walls, [2013].

[24] ANSYS inc. Ansys fluent, heat tranfer modeling, 15.0 release, lecture5: Radiative heat transfer, slide 5, surface to surface model, [2013].

[25] Michael Stueben. Twenty years before the blackboard, [1998].

[26] Wikipedia. https://en.wikipedia.org/wiki/kapton, [accessed Feb. 2017].

[27] ANSYS inc. Ansys academic research, release 17.2, help system, theory guide, [2013].

C

Acknowledgements

I start thinking about the Acknowledgements section three months before finishing the thesis. This is probably the only personal and private part of the entire dissertation. I have been reading Acknowledgments sections from dozens of theses, and, despite they were meant to be original and unique, they were all similar and stereotyped. I wanted to write something mine, not just copied and pasted from others. In my opinion, writing an Acknowledgements section is like make a gift: it doesn't matter the object itself, the real value of the gift is the personal time you have spent on it, thinking about it, building it or simply looking for the best choice; going to a shop just to buy a thing is not making a present. It's fulfilling a social convention. I don't want my Acknowledgement section to be merely a social convection. In the first chapter, I started this thesis with a sort of epigraph, introducing with a metaphor the idea of the voyage; in the final part of the main body, writing the result chapter, I was mental-swimming from a rock to another. So I thought that a good way to close the metaphor chain was to imagine me on a ship, sailing from an harbor (the first chapter) to the other (the last chapter). In this context, it was easy for me identify the people who help me as the crew of the vessel. A ship without crew can't sail, so, I would like to thank all the members. Without them, I couldn't have finished my thesis work.

My Supervisor, Professor Davide Del Col, was the harbor Master. Without his help and his academic presence, the ship couldn't have left the harbor and reach the other one.

My co-Supervisor, Eng. Corrado Gargiulo, was the Captain. Staying in the cockpit, he leaded the ship through the sea, and with his endless patience he faced the storms, keeping the ship on the target path.

Eng. Elisa Laudi was the Vice-Captain, out of the cockpit. She didn't have an established place inside the ship to stay, because during the whole voyage she has been exactly where her help was needed. Remarkable, Indispensable.

The CERN CFD-team represented the oars. Without their computer, my simulation couldn't have finished. A special mention to Aniko and Eugenia: it's always nice to find people like them, willing to assist with precious advices, no matter the time needed.

Eng. Andrea Francescon was for me the skilled sailor: with his wide experience, he always had a solution for every tipe of problem.

Andrea Dainese and Massimo Benettoni (INFN Padova) were the traders in the ship; at the beginning, their network of knowledge has been essential.

Massimo, Alèxandros, Claudia, Munir and Sofia were my shipmates. They create a very nice environment onboard, especially during the yolo-lunch in the galley (R1).

Finally, there was my family. My father, my mother and my sister were as invisible as vital. They were the ropes that let the ship navigate. They represent my bonds. My girlfriend Giulia instead pushed me every time I needed and make me move forward, despite the distance. She has been the Wind.

Thanks to all.

Lists of Figures and Acronyms

List of Acronyms

ALICE	A Large Ion Collider Experiment
ATLAS	A Toroidal LHC ApparatuS
BP	Beam Pipe
CERN	Conseil européen pour la recherche nucléaire
CFD	Computational Fluid Dynamics
CMS	Compact Muon Solenoid
COSS	Conical Structural Shell
CP	Cold Plate
CYSS	Cylindrical Structural Shell
DB	Detector Barrel
DBN	Detector Barrel Nozzles
DCaL	Dijet Calorimeter detector
DoF	Degree of Freedom
EMCaL	Electro Magnetic Calorimeters
EW	End-wheel
FIT	Fast interaction Trigger system
FPC	Flexible Printed Circuit
GEM	Gas Electron Multiplier detector
HIC	Hybrid Integrated Circuit
HMPID	High-Momentum Particle Identification Detector
HS	Half-Stave
IB	Inner Barrel

Table C.1: Acronyms/1

IEN	Inlet End Wheel Nozzles
IP	interaction point
I-SB	Inner Service Barrel
ITS	Inner Tracking System
L0, 1, 2	Inner Layer 0, 1, 2
L3, 4	Middle Layer 3, 4
L5, 6	Outer Layer 5, 6
LHC	Large Hadron Collider
LHCb	Large Hadron Collider beauty experiment
LS2	Long Shutdown 2
MAPS	Monolithic Active Pixel Sensor
MFT	Muon Forward Tracker detector
OB	Outer Barrel
O-SB	Outer Service Barrel
PB	Power Bus
PHOS	Photon Spectrometer detector
PID	particle identification
PP	Patch Panel
PW	prepreg woven
QGP	Quark-Gluon Plasma
RS	Reference System
SB	Service Barrel
SBN	Service Barrel Nozzles
SDD	Silicon Drift Detector
SF	Space Frame
SPD	Silicon Pixel Detector
SSD	Silicon Strip Detector
TID	Total ionizing dose radiation
TOF	Time-of-Flight detector
TPC	Time Projection Chamber detector
TRD	Transition Radiation Detector
YETS	Year End Technical Stop

Table C.2: Acronyms/2

List of Tables